Investigation of the Excitation Spectrum of ^{8}He via Deuteron Inelastic Scattering

By

Gurmukh Singh

A Thesis Submitted to Saint Mary's University, Halifax, Nova Scotia in Partial Fulfillment of the Requirements for the Degree of Master of Science in Applied Science

(Department of Astronomy and Physics)

2023, Halifax, Nova Scotia

Approved: _____

Dr. Rituparna Kanungo (Supervisor)

Approved: _____

Dr. Ivana Damjanov (Examiner)

Approved: _____

Dr. Greg Hackman (Examiner)

Approved: _____

Dr. David Hornidge (External Examiner)

Date: 12th December, 2023

Abstract

Investigation of the Excitation Spectrum of ^{8}He via Deuteron Inelastic Scattering

By Gurmukh Singh

Halo nuclei form due to weak binding at extreme proton-neutron asymmetries near driplines and these uncovered alterations in nuclear shell structure. These halos can exhibit a phenomenon known as a soft dipole resonance. It was postulated that 2^{+} state of ^{8}He may be a mixed with low-lying soft dipole resonance state but it is an unsettled issue. In this work, the deuteron inelastic scattering off a neutron halo nucleus, ^{8}He, has been studied in inverse kinematics at the IRIS facility at TRIUMF. This study presents findings of first excited state at E = 3.57 $\pm$ 0.02 MeV with resonance width of 0.64 $\pm$ 0.06 MeV along with the ground state. The possibility of absence of low-energy soft dipole resonance in the extracted excitation spectrum might be due to the stronger binding of ^{8}He. There is also no intruder s-orbital known in ^{8}He which can allow L=1 particle-hole excitation.

12th December, 2023

Acknowledgements

I would like to express my sincere gratitude and appreciation to everyone who contributed to the completion of this thesis. I am incredibly grateful to my supervisor, Prof. Rituparna Kanungo, for her invaluable guidance, scholarly insights, and unwavering support during this research. Her expertise and encouragement have played a crucial role in shaping this work. I am sincerely grateful to my thesis committee members Dr. Ivana Damjanov and Dr. Greg Hackman for their support during my research.

I would like to thank Mukhwinder Singh and Nikhil for their constant support, engaging discussions, and unwavering encouragement throughout the different stages of this research. I want to thank the IRIS collaboration for sharing their knowledge and insight throughout this project. I am also thankful to Saint Mary's University for providing the necessary resources and facilities that were essential to the successful completion of this study.

My deepest appreciation goes to my family for their love, understanding, and unwavering support throughout my academic journey. Lastly, I want to thank all the individuals, whose names might not be mentioned here, but whose support and encouragement were vital in completing this thesis. Thank you all for being part of this remarkable journey.

Contents

List of Figures

List of Tables

Chapter 1

Introduction

The development of radioactive nuclear beams has brought much attention to nuclei far from stability. This gave access to and enabled the production of these unique nuclei at sufficient rates [1, 2]. With this, nuclear physics research has been driven towards to understand how matter is structured at large neutron to proton imbalance. It is of interest to conduct experimental investigations of these nuclei in order to understand these exotic structures. Studying neutron-rich nuclei uncovered unexpected findings, such as vanishing of shell closures and the formation of neutron halos [3]. These observations indicated a lack of comprehensive understanding regarding the interaction among nucleons, i.e. the strong nuclear force. Neutron halos are defined as clusterization into a "core" having a moderately compact density distribution following known predictions from stable nuclei and one or more neutrons whose density distribution extends far from the core, into the classical forbidden region. ^{8}He is one such exotic nucleus at the neutron drip-line with largest neutron to proton ratio. This thesis work addresses the investigation of the excitation spectrum of the most neutron-rich exotic nucleus,^{8}He using an isoscalar probe, deuteron.

1.1 Physics Background

Nuclei are one of the most fundamental building blocks in our universe. An atom is formed when a distribution of electrons surrounds the protons and neutrons. An attractive electromagnetic force (Coulomb force) between a positively charged nucleus and negatively charged electrons binds an atom. The average size of an atom is roughly 10^{-10} m. There are almost 100 such elements formed from these atoms whose chemical and physical properties are known in great detail. The nucleus is a bit mysterious. The short-range attractive force binds protons and neutrons together, and the interplay between this nuclear force and the repulsive electromagnetic force among positively charged protons results in the formation of stable nuclei with specific combinations of neutrons and protons. If a nucleus has too few or too many neutrons for the number of protons it contains, the delicate balance can be disrupted, and the nucleus may become unstable. These nuclei lie away from the region of stability on the nuclear chart. The study of nuclear structure aims to understand how the atomic nucleus, composed of protons and neutrons, exhibits properties such as mass, energy levels, and radioactive decay. These characteristics emerge from the strong nuclear interaction between nucleons. Researchers investigate the strong nuclear interaction between nucleons to unravel the underlying mechanisms that give rise to these nuclear properties and behaviors.

In 1934, Yukawa postulated the particle exchange mechanism between nucleons (protons and neutrons). This mechanism results in an attractive force and provided the answer for the stability of the atomic nucleus [4]. The lightest meson, pion was discovered later and confirmed the the exchange mechanism of particles between the nucleons and this exchange mechanism results in the attractive force [5]. This force is strongest among four fundamental forces and this force is called the strong force.

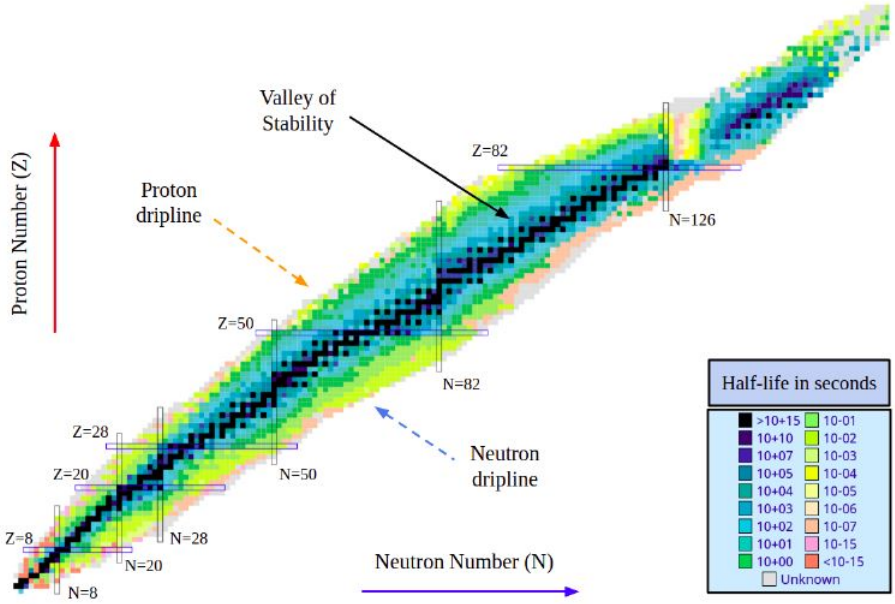

Figure 1.1: Nuclear chart(Segre chart).The nuclei are color-coded according to their half-lives (in seconds). The stable nuclides (black color) create the valley of stability. The upper and lower extremes of the chart define the proton and the neutron drip lines. The magic numbers for proton number (Z) and neutron number (N) are marked with horizontal and vertical black boxes, respectively. The data is taken from the National Nuclear Data Center (NNDC) at Brookhaven National Laboratory (BNL) [6].

The nucleus is bound by this balance between the repulsive electromagnetic force and the attractive strong force. The specific combinations of neutrons and protons that result in stable nuclei are a consequence of the complex interactions between the strong nuclear force and the electromagnetic force. About 280 stable (very long-lived) nuclear species are found in nature but, according to current estimates, from 5000 to 7000 bound nuclei should exist in the universe [7]. Stable nuclei are restricted to a narrow region known as the Valley of Stability on the nuclear chart

(or Segre chart) shown in Figure 1.1. The nuclear landscape is dominated by unstable nuclei and the edges of the nuclear chart are known as the drip lines. They indicate the point at which nuclei are no longer stable against spontaneous particle emission. Such nuclei with very weak binding and having large neutron to proton ratios possess exotic properties are referred to as exotic nuclei.

1.2 Nuclear Models and their Limitations

Yukawa's particle exchange mechanism sets the range of nuclear force due to the mass of exchange particle on the basis of the Heisenberg uncertainty principle, and compared to the electromagnetic and gravitational forces, the nuclear force operates over a limited distance. If it had a longer reach, we would anticipate an increase in the binding energy of nuclei as the mass number increases. The nucleons interact primarily with their close neighbors because this range is even smaller than the size of the nucleus. In addition, the measured nuclear binding energies demonstrated that the nuclear interaction saturates, resulting in nearly constant interior nucleon density. The liquid drop model explains binding energy by considering the nucleus as a droplet of liquid held together by a balance between the attractive strong nuclear force and the repulsive Coulomb force. The binding energy is a measure of the stability of the nucleus and depends on factors such as surface tension and the interplay between attractive and repulsive forces [8]. The liquid drop model is able to explain the global properties of nuclei, such as binding energies, sizes, and shapes. The liquid drop model provides a reasonable approximation for the overall behavior of nuclear binding energies, but it has limitations. It does not account for the shell structure of the nucleus indicating the presence of closed shells at some protons and neutron numbers. The large two proton and two neutron separation energies and the zero electric quadrupole moment (spherical shape) for these

magic nuclei provide evidence of shell structure inside the nucleus [9]. The shell closures were observed at 8,20,28,50,82 and 126, which are referred to as the ”magic numbers”.

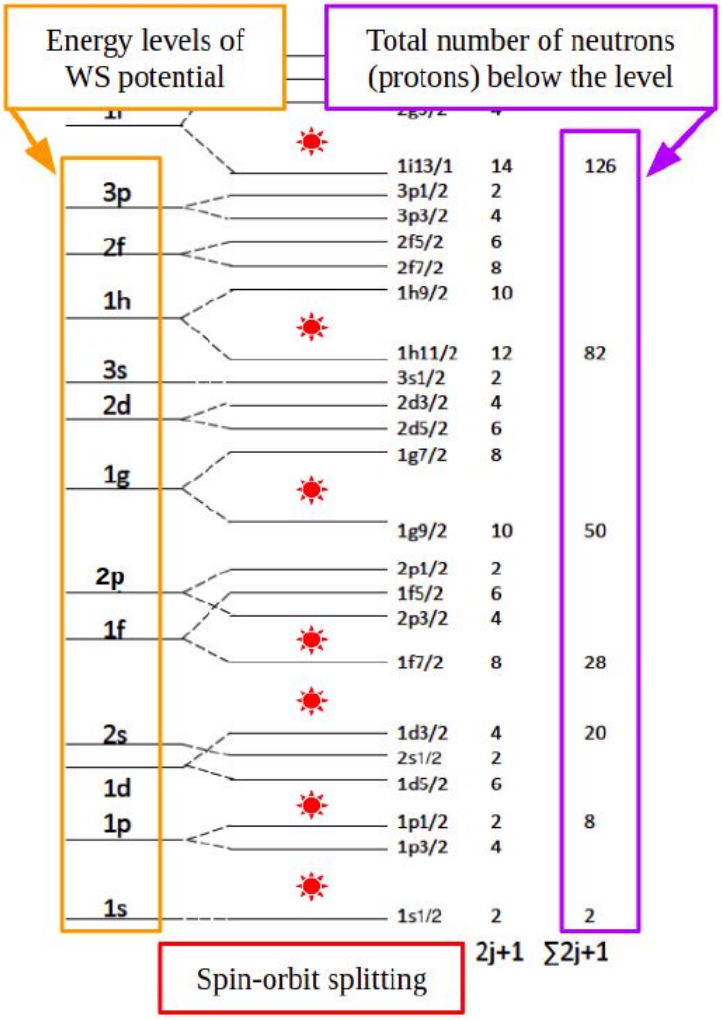

Figure 1.2: The highlighted energy levels on the left are of Woods-Saxon potential(WS) without the spin-orbit term. The addition of the spin-orbit term splits the energy level into two (except *s*-orbital). Individual energy levels can hold $2j + 1$ nucleon. The red marker indicates the major shell gap at the magic number [10].

These nuclei are strongly bound as compared to others nuclei. The sudden decrease in the neutron-capture cross section and the nuclear charge radius at magic number strengthened the idea

of shell existence [11]. The atomic shell theory and nuclear shell model work on similar concepts. The atomic shell model states that atoms' electrons orbit the nucleus in different shells [12, 13]. Similarly, according to the nuclear shell model, protons and neutrons are distributed in discrete shells [3, 14]. According to the shell model, an effective potential created by every other nucleon inside the nucleus influence the movement of each nucleon. If this assumption holds true, it can be inferred that the nuclear potential is approximately proportional to the density of nuclear matter. Application of the shell model used to describe the nucleus by assuming spherically symmetric potential i.e. Woods-Saxon potential ($V_{WS}(r)$). The shape of nuclear potential is an empirical form;

$$V_{WS}(r) = \frac{-V_0}{1+e^{(\frac{r-R}{a})}} \tag{1.1}$$

where $R = r_0 A^{\frac{1}{3}}$ is nuclear matter radius, V_0 is potential well depth ($\approx$ 50 MeV), A is the mass number, r_0 is constant = 1.25 fm, and a is surface diffuseness ($\approx$ 0.5 fm). By incorporating the spin-orbit term in a nuclear potential, the magic numbers were explained by M.Mayer [15] and J.H.D Jensen et al [16].

$$V(r) = \frac{-V_0}{1+e^{(\frac{r-R}{a})}} + W(r)\vec{L}\cdot\vec{S} \tag{1.2}$$

where $\vec{L}$ and $\vec{S}$ are the orbital angular momentum operator and intrinsic spin operator of nucleons, respectively. The second term in equation 1.2 is the spin-orbit potential where $W(r) = \frac{1}{r}\frac{dV_{WS}(r)}{dr}$. Figure 1.2 depicts the energy levels of the Woods Saxon potential and their splitting as a result of spin-orbit coupling. Each energy level is capable of accommodating $2j$+1 nucleons, where j is the total angular momentum. When the shell is completely filled, the nuclei tend to have exceptionally strong binding and stability. Magic numbers are the number of nucleons required to form a closed shell. The shell model description of the nucleus was an incredible achievement. For exotic nuclei,

usual structures are associated with the changes in nuclear orbitals deviating unexpectedly from our conventional knowledge. It was seen that re-arrangement in nuclear orbits starts to take place, changing the shell structure [17]. The shell evolution was explained by including contributions coming from tensor, central, and three-body forces in exotic nuclei [18]. The protons and neutrons present in different shells can also have interaction between them and this interaction can explained by tensor, central and three-body forces.

1.3 Properties of Exotic Nuclei

Studying the various properties of exotic nuclei is currently a hot topic in nuclear science. It can not only reveal the nature of short-range nuclear forces but can also explain the origin of chemical elements in nucleosynthesis [19]. As discussed in the first section exotic nuclei are those nuclei that contain many more or many fewer neutrons than a stable isotope of the same element. They lie far away from the stability line in the chart of nuclei, so in this region, nucleons (usually neutrons) are very weakly bound, giving rise to exotic properties like the formation of halo and skin. The difference between halo and skin is defined in subsection 1.3.3. In the absence of confining Coulomb barrier, these features are prominent in neutron-rich nuclei compared to proton-rich nuclei.

1.3.1 The First Measurement of Halo Nuclei

In 1985, at Lawrence Berkeley Laboratory, Tanihata, and his collaborators carried out an experiment using primary beams of ^{11}B and ^{20}Ne at 800 MeV per nucleon. They produced He and Li isotopes by projectile fragmentation with Be target and reported measurements of interaction cross

sections of Helium isotopes - ^{4,6,8}He [2], Lithium isotopes - ^{6,7,8,9,11}Li, and Beryllium isotopes - ^{7,9,10}Be. Same measurements were done for ^{11,12,14}Be in 1988 [20]. It was found that the measured cross-sections were much larger than expected for some of these isotopes. For ^{11}Li nucleus, measured root mean square (r.m.s.) matter radius was about 1.5 times larger than a stable nucleus which did not follow commonly used estimation of the radius being proportional to $A^{1/3}$, where A is the mass number. The root mean square matter radius of ^{11}Li is comparable to the ^{208}Pb and this evidence of a long tail in the nuclear matter distribution, i.e. halo, led to further experiments and studies of the halo phenomenon.

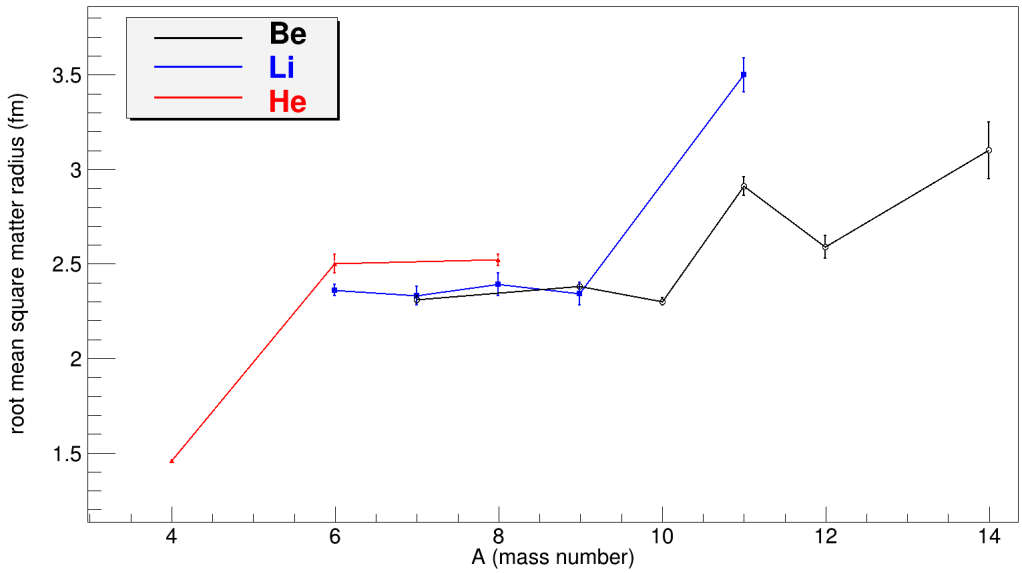

Figure 1.3: Root mean square (r.m.s.) nuclear matter radii of Lithium, Helium, and Beryllium isotopes, as obtained by Tanihata et al. [2, 20]. ^{11}Li, ^{6,8}He, and ^{11,14}Be have a much larger radius than their other respective isotopes.

From Tanihata's experiment, Hansen and Johnson introduced the term "halo" for ^{11}Li nuclei which have large radii due to the low binding energy of the last neutron pair [21]. The existence of halo nuclei was confirmed after measuring the enhancement in cross-section for electromag-

netic dissociation, momentum distributions, and β-decay [22]. The halo nuclei have wider density distribution which gives narrow momentum distribution. There is much large probability of beta-delayed neutron emission in neutron rich halo nuclei. The daughter nucleus after β-decay is in an excited state and the energy of that excited state is above the neutron separation energy, then the emission of a neutron becomes energetically possible.

1.3.2 The Concept of a Neutron Halo

The average nucleon separation energy for the last neutron of stable nuclei is about 6-8 MeV. However, for neutron-rich nuclei lying near the dripline, it is very small; in some cases, it is less than 1 MeV. The neutron halo shows an extremely long tail of neutron density distribution of a loosely bound system. Neutrons being electrically neutral and do not experience the same electromagnetic repulsion that protons do and potentially tunnel through the energy barrier created by the strong nuclear force. To further understand halo phenomena, Hansen and Jonson gave an explanation for a two-neutron halo by assuming a core of ^{9}Li as a square-well potential that binds a dineutron(two neutrons that are strongly correlated) [21]. This model allows quantum tunneling of two weakly-bound valance nucleons through the wall of the core potential barrier due to very low two-neutron separation. The wave function associated with the nucleons outside the potential is [23]

$$\Psi(r) = \left[\frac{2\pi}{\kappa}\right]^{-1/2} \frac{\exp(-\kappa r)}{r} \left[\frac{\exp(-\kappa R)}{(1+\kappa R)^{1/2}}\right] \tag{1.3}$$

where R is the width of potential κ determines the slope of the density tail also called the decay parameter and related to two-neutron separation energy ε by:

$$\kappa = \frac{2\pi \times (2\mu\varepsilon)^{1/2}}{h} \tag{1.4}$$

where μ is the reduced mass of the two neutron-core system. The density distribution of the neutron is:

$$\rho(r) = |\Psi(r)|^2 \propto \frac{\exp(-2\kappa r)}{r^2} \tag{1.5}$$

The separation energy is approximately 6-8 MeV for stable nuclei, hence slope factor does not change for these nuclei. The exotic nuclei have separation energy ranging from few hundred keV to few MeV, so this slope factor dominates. Decay parameter κ decreases with separation energy ε, and the tail of the neutron distribution will extend. As shown from the above relation, the nuclear halo can be identified by an extended nuclear distribution. The additional criterion for the formation of the halo is that the valance neutron(s) must be in a *s*- or *p*- state because the centrifugal barrier increases for higher *l*-values [24]. The term, Borromean, was first coined by Zhukov et al. [25] to denote a bound three-body system (core $+n+n$) for which no binary subsystem (core + n or $n+n+n$) is bound.

1.3.3 Examples of Halo nuclei

There are many types of halo nuclei depending on the type of internal system like one-neutron, two-neutron, or four-neutron. Examples for one neutron halos are ^{11}Be and ^{19}C, two-neutron halos or Borromean nuclei are ^{6}He,^{11}Li, (^{14}Be,^{17}B,^{22}C) and four-neutron halos or double Borromean nuclei are ^{8}He and ^{19}B. Figure 1.4 shows different neutron halo systems. At the neutron dripline, a few other nuclei have properties that are very similar to those of the halo nuclei but excess of neutrons leads to the neutron distribution in the nucleus extending farther out from the core and that layer is called 'skin' and these nucleons are not as spatially extended as halo nucleons. The ^{8}He is a neutron skin nucleus. Tanihata et al. [26] reported neutron skin thickness for ^{8}He of about 0.9 fm

from cluster-type model analysis of the interaction cross sections of two-neutron and four-neutron ^{4,6,8}He. Neutron halo refers to the large diffuseness of the neutron density distribution, whereas neutron skin refers to an increase in the half-density radius of the neutrons. Both give rise to an extended neutron surface. Consequently, the asymptotic behavior of the density for the halo state is more diffuse than that of the skin [27].

Proton halos are uncommon because, despite the attractive nature of nuclear force, the Coulomb potential between protons prevents halo growth. Consequently, the neutron halos are observed more than the proton halos and few example of proton halos are ^{8}Be,^{17}Ne [28].

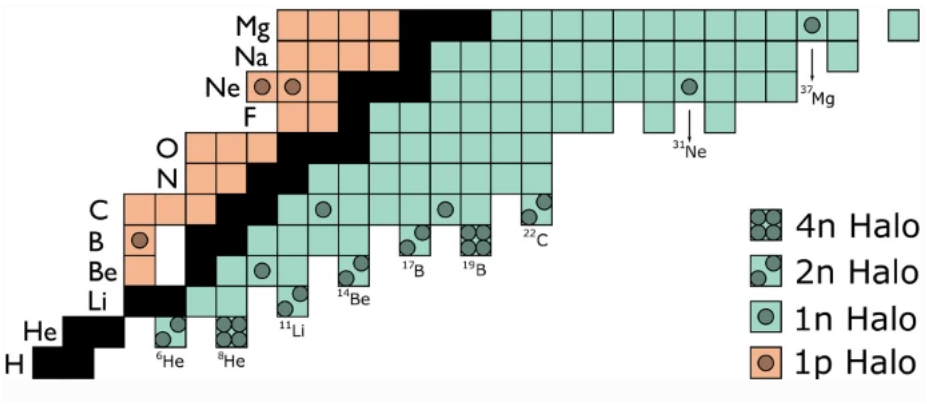

Figure 1.4: Low-mass region of the nuclear chart. Isotopes marked with a circle correspond to nuclei which show indications of a proton or a neutron halo. Stable nuclei are represented by grey blocks. The data is taken from the National Nuclear Data Center (NNDC) at Brookhaven National Laboratory (BNL) [29].

1.4 Concept of Excited States

The shell model is among the most effective theoretical explanations of nuclear structure. The shell model is predicated on the notion that, like electrons in an atom, (nucleons) protons and neu-

trons, occupy energy levels or shells within the nucleus. Protons and neutrons are both subject to the same quantum rules because they are fermions with half-integer spins. According to the Pauli exclusion principle, which states that no two nucleons can occupy the same quantum state simultaneously, the ground state of a nucleus is the lowest energy configuration where the nucleons fill the available shells. Nucleons occupy nuclear potential energy levels in the ground state in order to minimize total energy without violating the Pauli principle. Protons and neutrons must therefore adhere to the Pauli exclusion principle separately from one another.

Each nucleus has well-defined energy levels and these energy levels can be determined by measuring the excitation spectrum. Ground state as well as excited states are characterized by quantum numbers such as spin, parity, and angular momentum. Excited states can have different properties for different nuclei, so they need to be measured by nuclear reactions and radioactive decay. These states can be bound or unbound and unbound states are called resonance states.

In nuclear spectra, excited states can originate from three types of excitation modes which are independent particle excitation, vibrations, and rotations. The excitation of individual nucleons is independent particle excitation while the latter two involve the collective motion of the nucleons in the nucleus. To identify the multipole of excitation, the cross-section is measured and then compared with different multipoles to see which mode fits best with the experiment.

1.5 Known Properties of ^{8}He

There have already been numerous studies on the ground state of ^{8}He. There is very limited information when it comes to the experimental investigations of the excited states. The existing

results are statistically limited or even contradictory to one another. Using the variational Monte Carlo method, theoretical calculations place the lowest 2^+ state around 2.5-2.8 MeV and a 1^+ state around 3.2-4.4 MeV [30]. Oertzen et al. studied the spectrum of ^{8}He using ^{9}Be(^{13}C,^{14}O)^{8}He multiple-nucleon transfer reaction. This study was conducted at the Hahn-Meitner-Institute using ^{13}C beam of energy 337 MeV. The reactions were observed using a Q3D-magnetic spectrometer. Along with the ground state, for the very first time, the first excited state (2^+) was observed near 3.59 MeV with resonance width (Γ) (FWHM) = 0.80 MeV [31].

Later, in 1995, secondary ^{8}He beam was produced using primary ^{16}O beam at the RIPS facility in RIKEN. Using invariant mass spectroscopy from the reaction $p(^8\text{He},^8\text{He})p$ at 72 MeV/u, the first excited state was observed at 3.55 $\pm$ 0.15 MeV and with a width (Γ) (FWHM) of 0.5 $\pm$ 0.35 MeV. By measuring the angular distribution, the spin of the first excited state was confirmed to be 2^+. Other than that for the first time there was an indication of the existence of another excited state at 5.6 MeV [32].

T. Nilsson et al. [33] measured the neutron and ^{6}He momentum distribution from ^{8}He nuclear break-up reactions in a C target at 240 MeV per nucleon at the GSI in Darmstadt. They deduced the ^{8}He excitation spectrum from the invariant mass of ^{6}He + n + n channel and found the peak corresponds to resonance energy (E) around 3.72 $\pm$ 0.24 MeV and resonance width (Γ) (FWHM) 0.53 $\pm$ 0.43 MeV, which agree with the values quoted in Ref. [32]

J. Xiao et al. also conducted an experiment at RIKEN to study breakup reactions of the ^{8}He at 82.3 MeV/u with two different targets CH_2 and C. The first resonance peak was observed at 2.99 $\pm$0.02 and state with unknown spin was reported at 4.14$\pm$ 0.06 MeV [34].

Golovkov et al. conducted an experiment at JINR in which they used a primary beam of ^{11}B

ions at 34 MeV/u to produce secondary beams of ^{8}He and ^{6}He. The low-lying spectrum of ^{8}He derived from the transfer reaction ^{3}H(^{6}He,p)^{8}He was studied using the missing mass technique. Two excited states were observed, the first excited state having spin and parity of 2^{+} at energy around 3.6 MeV and the second one with spin parity 1^{+} at energy around 5.4 MeV. The third possible state was observed around 7.5 MeV but the nature of this resonance state was not discussed [35].

One can see that the first excited state 2^{+} of ^{8}He is defined with large uncertainty with excitation energy (E_{ex}) of about 2.7-3.6 MeV. The second excited state also has discrepancy associated with it. Some sources report it around 4 MeV and some report around 5.4 MeV which we have discussed. According to the theoretical predictions, the second excited state is assumed to be 1^{+} but spin parity is not known from experiments.It is highly likely that the 2^{+} state is combined or 'mixed' with a soft dipole (E1) mode, leading to the population of the 1^{-} continuum. This mixing of states may be responsible for the observed confusing or ambiguous results [36].

1.6 Soft Dipole Mode

The thickness of neutron skin of ^{8}He nuclei of about 0.9 fm was deduced in an experiment performed at RIKEN, by combined analysis of the interaction cross section (σ_I) and four neutron removal cross-section of ^{8}He projectile [26]. ^{8}He is best described as a five-body system (α + 4n) rather than a ^{6}He + 2n system using five-body cluster orbital shell model approximation (COSMA) [37]. It is thought that Soft Dipole Mode as depicted in Figure 1.5 may exist in ^{8}He, in which four neutrons acting as skin can oscillate against the core of the nucleus. Soft dipole resonance is a feature of halo nuclei and it is related to the low binding energy of the halo neutrons

which allows them low-frequency oscillations against the core creating low-lying dipole excitation.

The existence of soft dipole resonance in ^{8}He was reported at about 4 MeV in an early experiment done using Coulomb excitation [38, 39]. Golovkov and collaborators also populated the low-lying spectrum via a two-neutron transfer reaction ^{3}H(^{6}He,p)^{8}He and provided insight that there may be the possibility for the existence of soft dipole mode in ^{8}He.

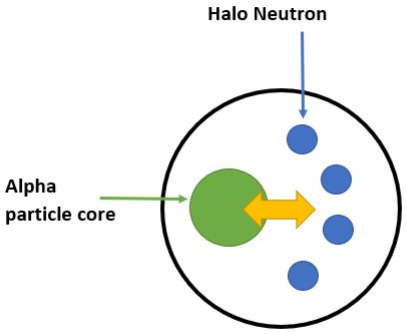

Figure 1.5: Soft Dipole Mode illustration in ^{8}He

But in this case, the resonance was observed at a slightly lower energy of about 3 MeV [35,36]. Markenroth et al. measured the angular distributions for the excitation spectrum in the region 0-6 MeV by using a fragmentation reaction of ^{8}He on the carbon target. The study used the distorted wave Born approximation (DWBA) to calculate the angular distribution for a dipole and quadrupole transition. It was found that there was the presence of a strong dipole mode in the excitation spectrum of ^{8}He after the measured angular distribution is compared with the calculated angular distributions. The observed state was of energy 4.15 MeV and the deduced spin was 1^{-} [38]. A recent ab initio work by Bonaiti, Bacca, and Hagan [40] favors the possibility of soft dipole mode in ^{8}He while the theoretical covariant density-functional theory (DFT) framework disfavors this [41].

In the recent study conducted at the IRIS facility at TRIUMF using inverse kinematics to study the inelastic scattering of ^{8}He with a solid hydrogen target a resonance state (2^{+}) was observed at 3.54(6) MeV with width (Γ) (FWHM) = 0.89(11) MeV . The angular distribution of the resonance was measured and compared with the calculated angular distribution for dipole and quadrupole transitions using DWBA [42]. From this experiment, it was concluded that the measured angular distribution was not consistent with the soft dipole mode. This study was not able to find any signature of the soft dipole resonance as predicted by Markenroth et al. near the 2^{+} state. A recent inelastic scattering measurement of the halo nucleus ^{11}Li with a solid deuterium target at IRIS gave evidence of the existence of soft dipole mode at an excited state around 1.03 MeV when the measured angular distribution was compared with the DWBA calculation for dipole transition. Solid deuterium was used as a target and it has isospin zero so it acts as an isoscalar probe. Therefore, the observed dipole resonance was an isoscalar dipole resonance [43]. So, to investigate if an isoscalar resonance might exist in ^{8}He, one can use an isoscalar probe to excite such resonance.

The scientific motivation of this thesis is to investigate the possibility of the existence of the soft dipole resonance in ^{8}He through the ^{8}He(d,d') inelastic scattering reaction. Our aim is to extract the excitation spectrum and derive the differential cross-sections for elastic and inelastic scattering. The experiment was performed using the experimental facility IRIS at TRIUMF, Canada. The subsequent chapters of this thesis are organized in the following manner:

- Chapter 2 provides a detailed description of the experimental setup needed to investigate the ^{8}He$(d,d)^{8}$He and ^{8}He(d,d') elastic scattering and inelastic scattering respectively. The final section of this chapter is dedicated to discussing the essential electronics and data acquisi-

tion.

- In Chapter 3, we will discuss the methodologies employed to analyze the data acquired from our experiment. This encompasses detector calibration, determining the thickness of the solid D_2 target, particle identification on an event-by-event basis, counting the incident beam particles through an Ionization Chamber (IC) scalar, and counting the scattered elastic and inelastic deuterons to extract and derive excitation spectrum and the differential cross sections for elastic and inelastic scattering.

- In Chapter 4, we will discuss the results obtained and summarise the observations from our experiment.

Chapter 2

Experimental Setup

This chapter presents a description of the experimental setup used to carry out this study. This chapter gives overview about the production of radioactive ion beams using cyclotron and how the beam is identified using ionization chamber to identify the contaminants. Next, brief overview is provided about target formation, light particle detectors, heavy particle detectors and how data is collected using data acquisition system.

2.1 Radioactive Ion Beam Production at TRIUMF

The current generation of RIB facilities having high production rates, efficient and selective, such as the Isotope Separator and Accelerator (ISAC) facility at TRIUMF (TRI-University Meson Facility), provide an unprecedented opportunity to address key questions of current interest in nuclear astrophysics, nuclear structure physics, fundamental symmetries, and molecular and material science by providing a wide variety of intense beams of exotic nuclei. At ISAC, the ISOL (the isotope separation on-line) method is used to produce the short-lived isotopes by bombarding thick pro-

duction targets with a beam of up to 100 A of 500 MeV protons from the TRIUMF H^- cyclotron. After that, the reaction byproducts are delivered to an ion source. The desired species are obtained by electromagnetic separation after obtaining the desired charge state. In Figure 2.1, the various stages of beam production and delivery are schematically depicted.

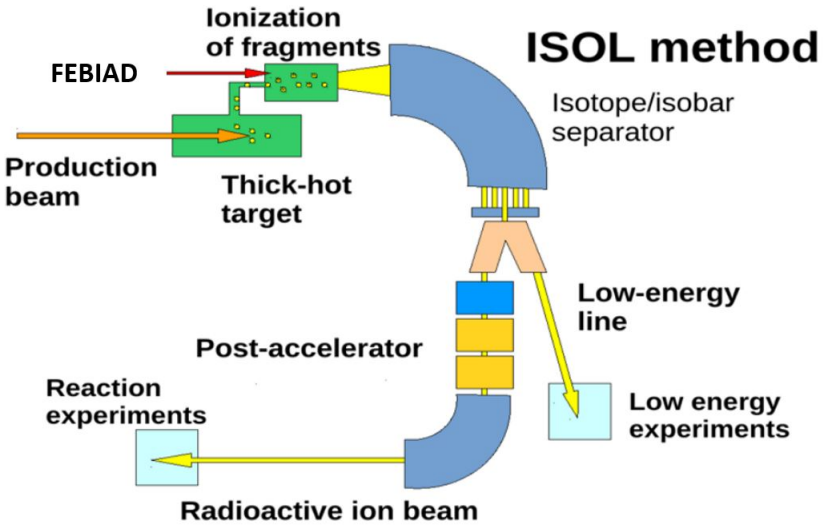

Figure 2.1: A schematic representation of the ISOL method [44].

In this experiment, the 500 MeV proton beam from the cyclotron at TRIUMF collided with a SiC target to produce the ^{8}He beam. The ^{8}He is separated from other isotopes using a mass separator and then re-accelerated using the ISAC-II superconducting linear accelerator to 8.35A MeV. After that, the re-accelerated beam is sent to the ISAC rare isotope reaction spectroscopy station (IRIS).

2.2 IRIS Facility

The IRIS facility is located in the ISAC II experimental area of TRIUMF and is dedicated to the study of charged particle reaction spectroscopy [45]. Its focus is on investigating elastic and

inelastic scattering, as well as transfer reactions, through the use of radioactive ion beams and hydrogen isotopes (H_2 and D_2) as targets. The resulting charged particles from this interaction are gathered and examined using various sets of detectors. The main components of this assembly are

- Ionization Chamber
- Solid H_2 or D_2 target
- Charged particle detectors
- Zero-degree beam detectors

Figure 2.2 displays the diagrammatic representation of the IRIS setup utilized in this study

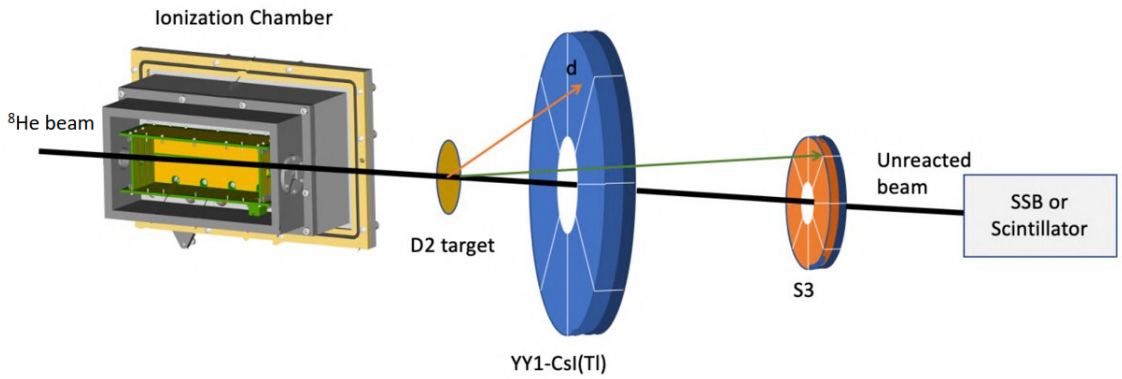

Figure 2.2: Layout of the IRIS experimental setup [46]

2.2.1 Ionization Chamber

This is first detector in the beamline, placed upstream of the target and it is filled with Isobutane (C_4H_{10}) gas at low pressure. Figure 2.3 shows the schematic for the IC. It measures the beam condition before it reaches the target. Its pressure can be controlled and can be set anywhere between 5 to 20 Torr. The ionization chamber serves two purposes. First, it counts the number of

beam particles, and second is to identify the isobaric constituents of the beam. Using the principle of energy loss for different particles having different atomic numbers while passing through the gas, these contaminants can be identified. After the radioactive ion beam (RIB) reaches the ionization chamber (IC), it traverses through a 40 nm SiN_2 window followed by 229 mm of isobutane gas. The energy deposit in the gas volume provides information on the beam particle identification. The objective of using the windows is to isolate the gas volume from the vacuum. The usage of these thin windows and low-pressure conditions guarantee minimal energy loss and small straggling within the ionization chamber. The interaction between the beam ions and the gas leads to the ionization of the gas, generating electron-ion pairs as a result of the energy transfer from the beam to the gas. Subsequently, these electron-ion pairs are collected by an anode and cathode, resulting in an electrical signal that undergoes processing through a pre-amplifier, shaping amplifier, and analog-to-digital converter (ADC) to record the data. Ultimately, the beam exits the IC through the secondary 50 nm SiN_2 window, after which it proceeds toward the scattering chamber.

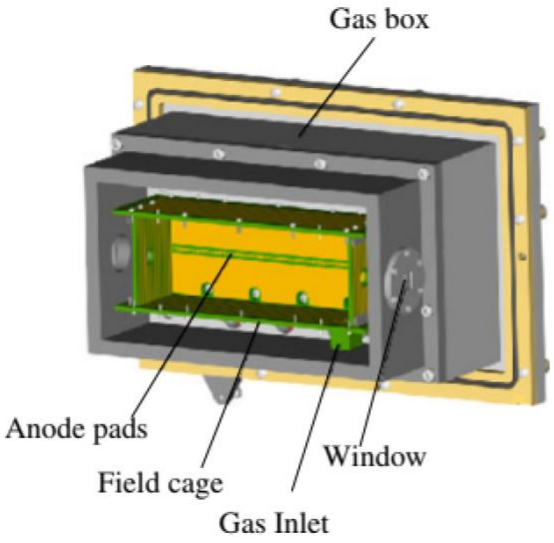

Figure 2.3: Schematic of the Ionization Chamber [45].

2.2.2 Solid H_2/D_2 Target

The use of solid-state deuteron target (SDT) is a unique and novel capability of IRIS for low-energy radioactive ion beam reactions. The solid deuteron target has a high density of target atoms implying more reaction centers which result in higher reaction yield. Another advantage is that in the case of a solid D_2 target, the background scattering from carbon nuclei will not be present. The scattered particles do not encounter any other material before reaching the detectors because the SDT only has a thin silver foil of about $\sim 4.5\ \mu m$ backing upstream of the target.

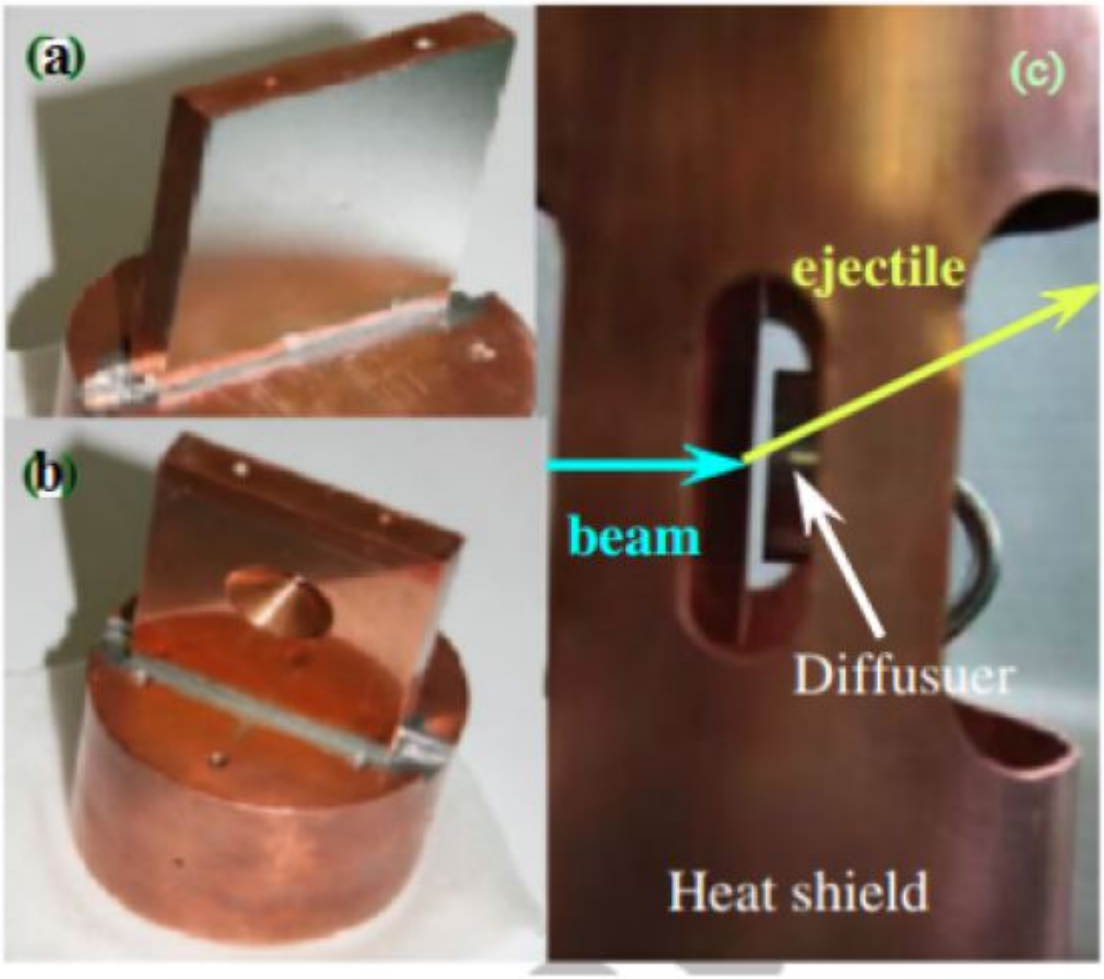

Figure 2.4: Solid H_2 target assembly [45].

The target cell made of copper is contained within a cylindrical heat shield of the target assembly to reduce the radiative heating of the target as shown in Figure 2.4. In the middle of the copper cell, a hole of diameter 5 mm is drilled. The cell is lined by a thin silver foil and the solid D_2 target is supported by this foil. The target cell is cooled to a temperature of 4 kelvin using a cryocooler equipped with a helium compressor. A diffuser is used to spray D_2 gas on the surface of the cold silver foil as shown in Figure 2.5. The targets that are used at IRIS typically have a thickness of between 50 and 100 μm. The D_2 target that was created for this experiment was approximately 50 μm, and the thickness of the target was achieved by controlling the gas volume.

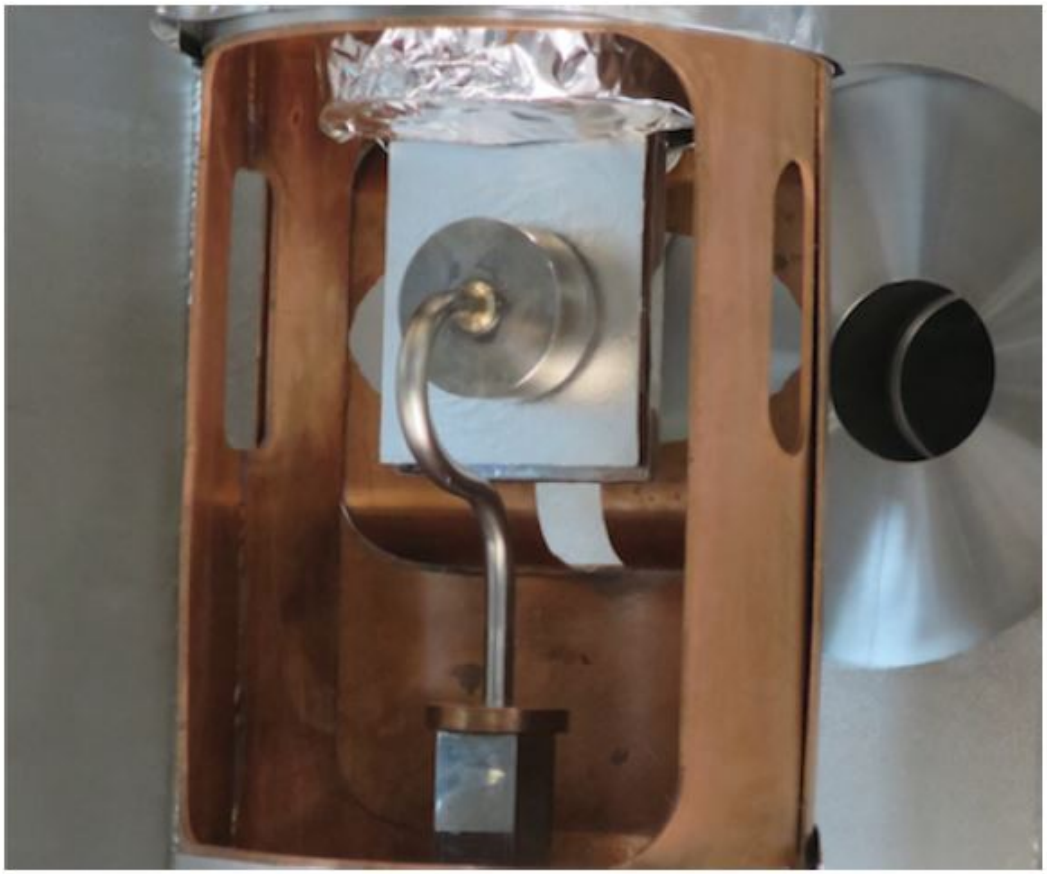

Figure 2.5: IRIS target assembly showing the diffuser in the upper position in front of the silver foil, placed within the copper heat shield [46].

In this work on ^{8}He(d,d'), the incoming ^{8}He beam first passes through the IC and then passes through the silver foil and then hits the solid deuteron target. The reaction is random and can take place anywhere inside the target. After the interaction point, the reaction products traverse the target's remaining thickness. By collecting data without a D_2 target, the background produced by fusion evaporation reactions on the Ag foil can be separately measured.

2.2.3 Charged Particle Detectors

The charged particle detectors used in the IRIS facility are designed to detect the reaction products of charged particles. The IRIS facility has two sets of detectors: one set is used to detect light target-like particles i.e. p, d, t, ^{4}He, etc, while the other set is used to detect heavy beam-like particles. Both sets of detectors use a combination of thin and thick detectors. The silicon array (YY1) - CsI detector is designed to detect target-like particles. This detector features a 100 μm thick segmented annular silicon detector array. It is composed of 8 azimuthal sectors, and each sector contains 16 rings, for a total of 128 segments that function as individual detectors, that measure a portion of the particle's energy, as well as its scattering angle. It is followed by a 12 mm thick annular CsI(Tl) array as shown in Figure 2.6. The setup consists of one sector of the YY1 detector and two CsI(Tl) crystals that are positioned behind it to detect particles of interest simultaneously with angle coincidence. The purpose of CsI(Tl) is to measure the rest of the light particle energy. The combination of YY1 and CsI(TI) therefore allows complete identification of the particle using energy-loss and total energy correlation referred to as a ΔE-E telescope. For this measurement, the angle coverage for the lighter particles was between 11° to 28°.

Figure 2.6 shows that the silicon detector and the CsI detector both have center holes. The

holes allow beam-like particles to pass through, and detectors made of both thin and thick double-sided silicon strips with active layer thicknesses of 60 μm and 500 μm, are positioned further downstream to detect these particles. These detectors are of S3 type and labeled as S3d1 followed by S3d2 as shown in Figure 2.7. On one side, it is divided into 32 sectors, and on the other, into 24 rings. The energy and angle of the scattered heavy particles are measured using this detector telescope.These downstream detectors cover the angles of θ_{lab} = 2° - 7°. S3d1 and S3d2 together act as an ΔE-E telescope to identify beam-like particles.

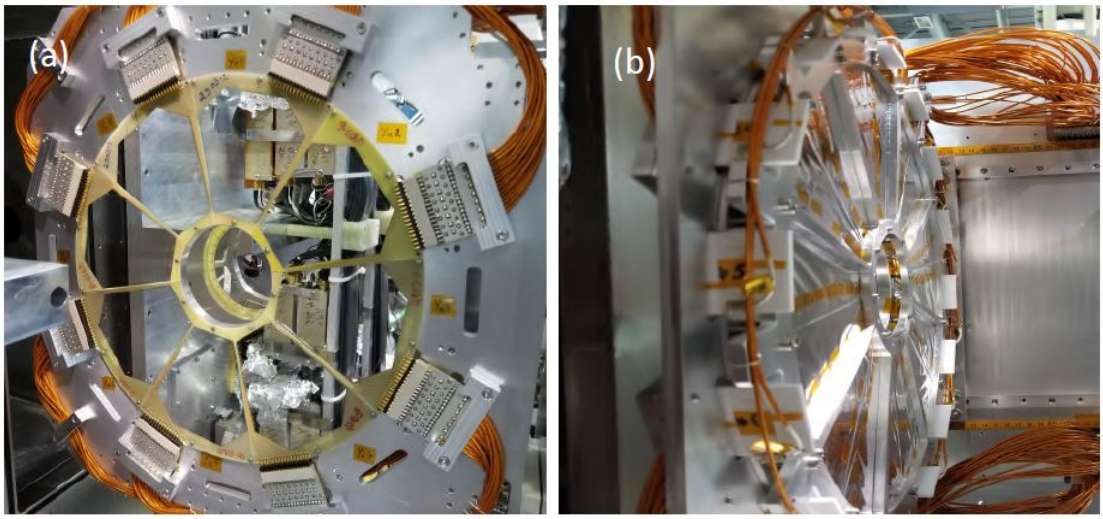

Figure 2.6: Detectors for target-like nuclei. (a) YY1 detector. (b) CsI(Tl) detector [45].

2.2.4 Scintillator and SSB Detectors

The detectors discussed in the previous sections are designed in an annular shape to enable the unreacted beam to pass through. The beam is then stopped by a YAP:Ce inorganic scintillator that is highly resistant to radiation. A photomultiplier tube is used to read the signal produced by this scintillator, which enables the detector to quantify the number of unreacted beam particles.

Throughout the experiment, the beam transmission across the experimental setup is observed by monitoring the ratio of particle counts in the ionization chamber to those in the scintillator. To measure the residual energy of the unreacted beam after passing through the target and hence to determine the thickness of the D_2 target, a silicon surface barrier (SSB) detector is employed as another zero-degree detector as shown in Figure 2.8. It is inserted in the beamline occasionally.

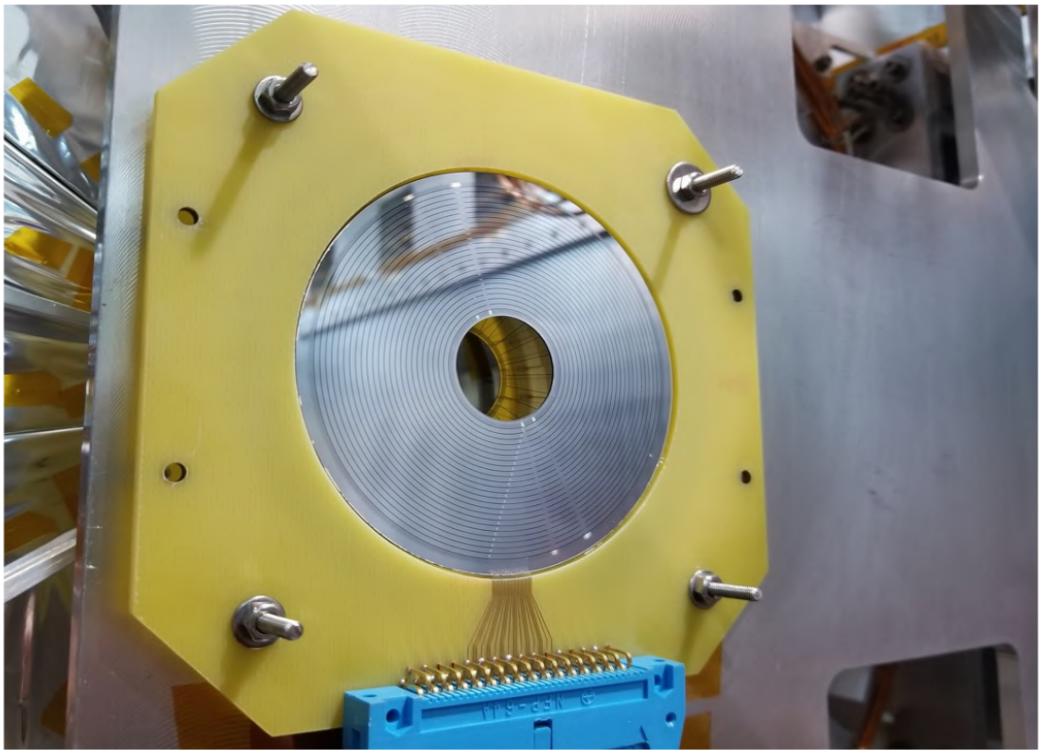

Figure 2.7: S3 detector [46]

2.2.5 Signal Processing at IRIS

The interaction of charged particles in the detectors produces a pulse of electric signal. This signal is then processed through a preamplifier and shaping amplifier. The main purpose of the preamplifier is to extract a voltage pulse from the detector. The charge-sensitive preamplifiers were employed for both the silicon and CsI(Tl) detectors. These preamplifiers produce an output volt-

age that is proportional to the total integrated charge in the pulse. The rise time of the output pulse corresponds to the charge collection time, while the decay time is determined by the RC time constant of the preamplifier. Low frequency components are blocked by the (RC) circuit, which improves signal to noise ratio. To minimize noise, the preamplifier is placed as close to the detector as possible to reduce capacitance from connecting cables. The preamplifier does not provide any pulse shaping, and the collected charge is directed to a shaping amplifier and discriminator unit. The MSCF-16 model [47] is used at IRIS, which is a 16-channel shaping/timing amplifier equipped with a leading-edge discriminator (LED).

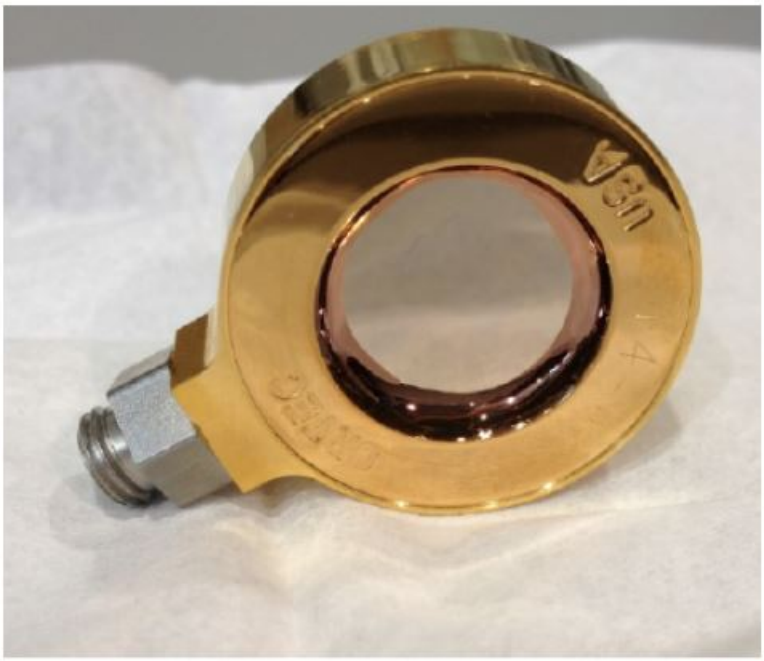

Figure 2.8: SSB detector [46].

In order to effectively store the information conveyed by the pulse, it must be converted from an analog signal to a digital one. The amplified energy signal received from the pulse shaper unit is directed to an analog-to-digital converter (ADC) to accomplish this conversion.

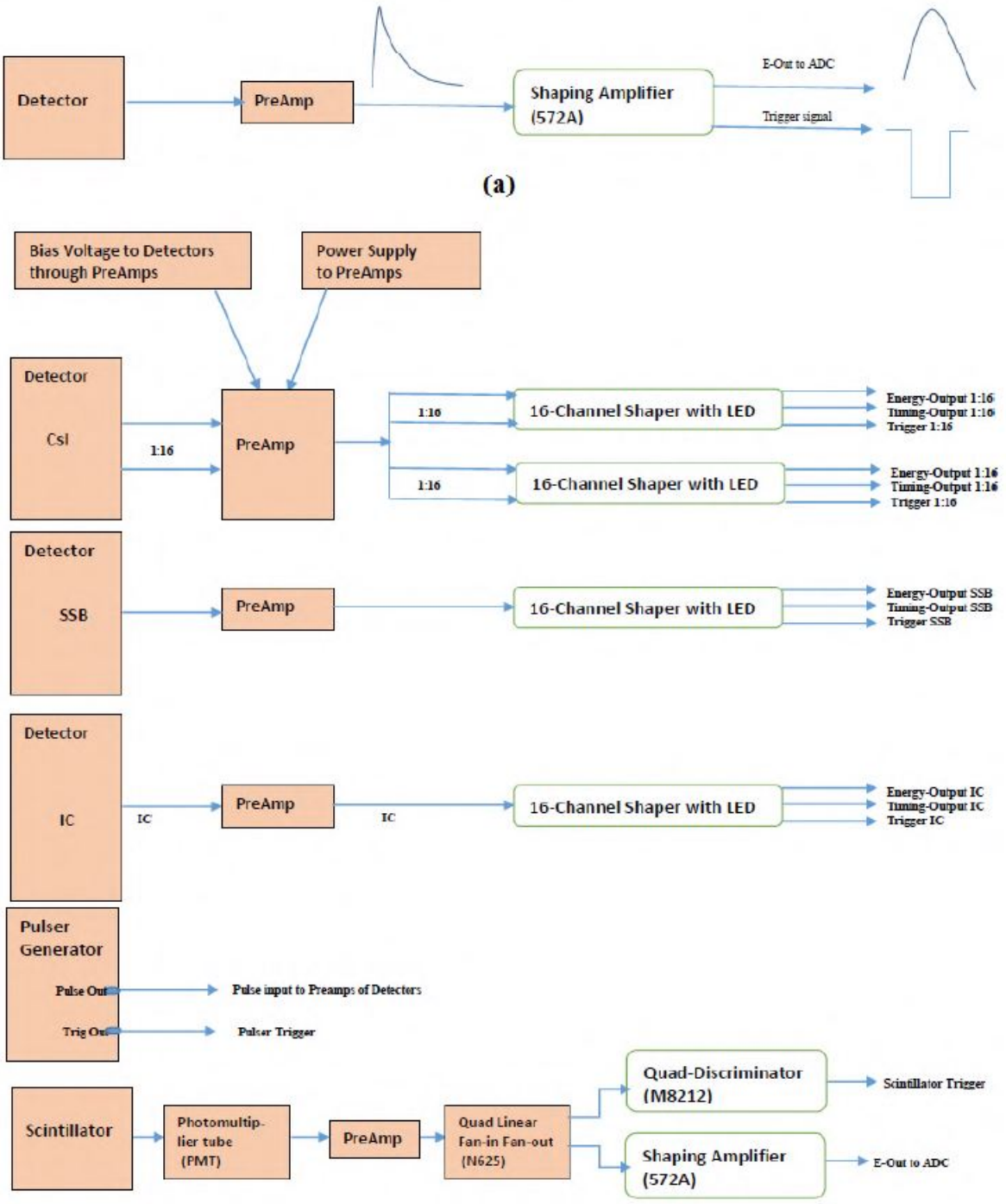

Figure 2.9: Pulse processing. (a) Output from a preamplifier unit and a shaping amplifier for a general detector.(b) Output from the shaping amplifier for CsI(Tl), SSB, IC, Pulser, and scintillator [46] [47].

The ADC unit converts the amplitude of an analog voltage signal into a proportional digital number. At IRIS, peak-sensing ADCs (model number MADC32) were employed, which have a full range of 4096 channels i.e. with 12-bit resolution. As we were primarily interested in analyzing the scattered particles detected by the YY1-S3 detectors, we performed a Logic-OR operation on the trigger signals obtained from the MSCF-16 unit of the YY1/S3 detectors to obtain a ”free trigger” signal. However, the data acquisition system (DAQ) cannot store all trigger events from the detectors because processing each event requires a finite amount of time. The accepted trigger is directed to the Quad Gate generator unit (M794) to acquire data in coincidence, which generates a gate pulse with a user-defined time window, telling the ADC when to start and stop taking data.

Chapter 3

Data Analysis

In order to extract the excitation spectrum of the ^{8}He nucleus, it is necessary to calibrate the various detectors discussed in the previous section. This chapter outlines the methodology employed to calibrate the detectors, and how the calibrated data was applied to extract the Q-value spectrum using the missing mass technique. It also discusses the determination of differential cross-sections for the ground state and observed resonance state.

3.1 Identification of Beam Particles

At the outset of the data analysis process, the initial step is to distinguish between particles in the beam with different atomic numbers but identical masses. This was accomplished by careful examination of the ionization chamber spectrum. The identification is based on the principle of stopping power, which is described by equation 3.1

$$\frac{-dE}{dx} \propto \frac{Z^2}{v^2} \tag{3.1}$$

The term $\frac{-dE}{dx}$ refers to the amount of energy that a particle will deposit per unit length of a material. Where v is the velocity and Z is the atomic number of the charged particles. The ADC spectrum measured by the IC is depicted in Figure 3.1. The spectrum indicates the presence of only one Gaussian peak, indicating that the ^{8}He beam was uncontaminated, with no other impurities present except for some background noise. A selection gate shown by two red vertical lines corresponds to $\pm$ 3σ region on the ^{8}He particles is used in further analysis to eliminate pedestal on the lower channels and pulsar signal on higher channels.

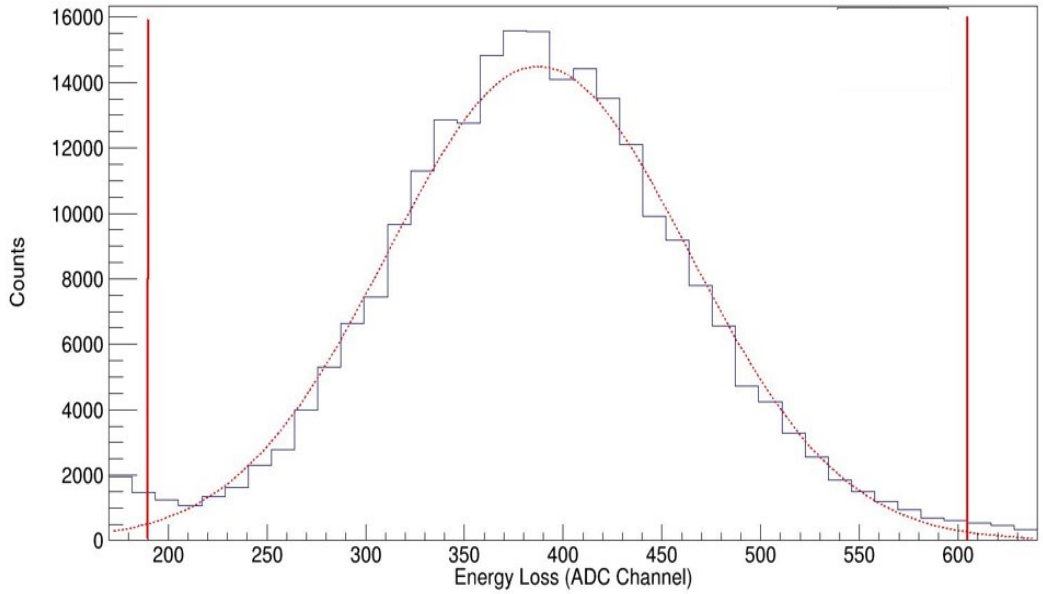

Figure 3.1: ADC spectrum of IC.

3.2 Detector Calibration

This section will focus on the detailed process of calibrating the energy of detectors, which serves as the foundation for data analysis. As previously mentioned, when a charged particle passes through a detector, it deposits a certain amount of energy, generating a voltage pulse. The detector

response is the correlation between the energy deposited by the radiation and the total charge or pulse height of the resulting output signal. IRIS uses peak sensing ADCs, where the peak voltage of the pulse is converted into a digital value. The digital value is known as the channel number. The process of converting these channel numbers into a physical quantity, such as energy, is known as calibration. The following linear equation was used for the calibration of the detectors:

$$E = g \times (c - p) \tag{3.2}$$

E corresponds to the energy that is deposited in the detector, c represents the channel number of the peak position in the resulting signal, p denotes the pedestal value, which is the channel number that corresponds to an energy deposit of zero, and g represents the gain, which is the factor that converts channel number into energy units. The unit of g is MeV/channel if the energy deposited is in MeV. Next subsections will present a detailed account of the calibration process for the YY1, S3, and CsI(Tl) charged particle detectors. To calibrate the YY1 and CsI(Tl) detectors, it is necessary to determine the D_2 target thickness, which is also discussed in this chapter. The Ag foil used for the D_2 target backing had a thickness of 4.5 μm and this Ag foil will be used to calibrate S3 detector using ^{8}He(^{107}Ag,^{107}Ag)^{8}He.

3.2.1 Calibration of S3 Detectors

As mentioned in the previous chapter, the S3 detector telescope consists of two detectors, namely S3d1 of thickness 60 μm, and S3d2 of thickness 1 mm. While each detector requires individual calibration, the calibration procedure is the same for both. To calibrate the S3 detectors, experimental data obtained from the elastic scattering of ^{8}He particles from the Ag foil was utilized. This data was collected in the absence of the D_2 target. The telescope is capable of isolating elastic

events, which can then be used for calibration purposes. Figure 3.2 illustrates the energy deposited in the S3d1 versus S3d2 detector, with the red polygon indicating the gate used to isolate ^{8}He elastic events.

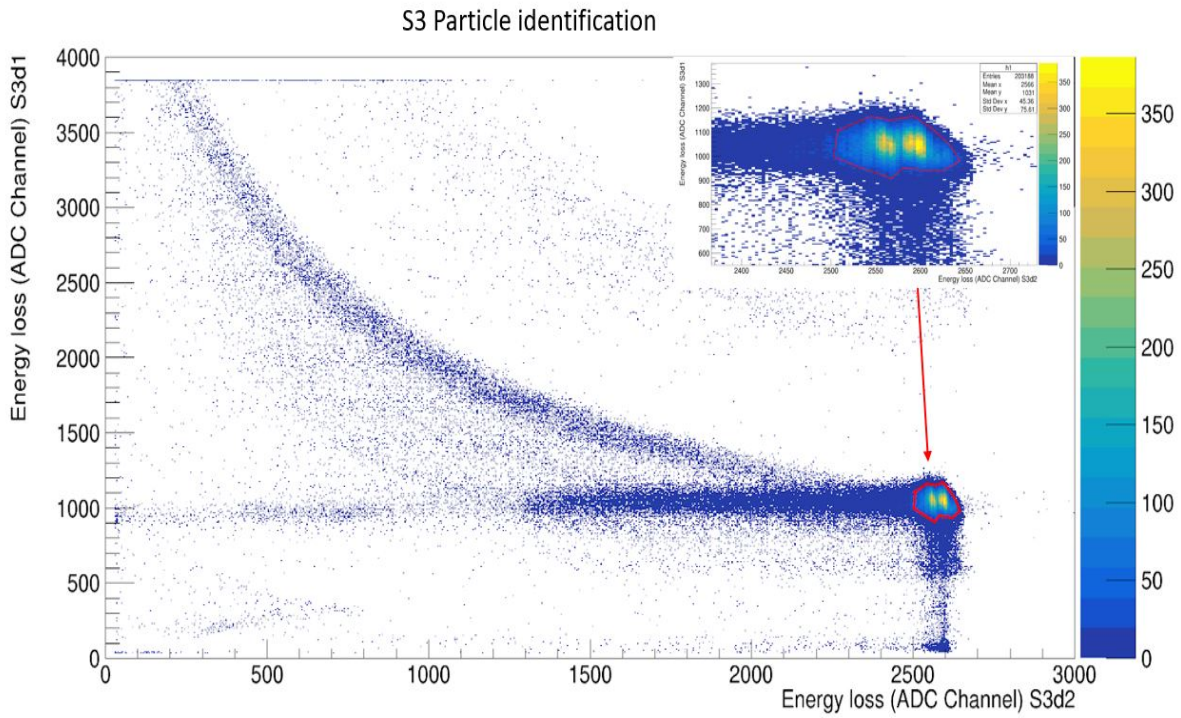

Figure 3.2: The ΔE-E telescope for the S3 detector. The red polygon is the gate for the elastically scattered ^{8}He events.

The energy loss of the incoming ^{8}He beam in the IC before scattering was accounted for, and the average probability of the scattering location within the Ag foil was assumed to be at the midpoint of the foil thickness.

Additionally, the energy loss of the scattered ^{8}He particles in the dead layers of the S3 detectors was taken into account during calibration. Both the S3d1 and S3d2 detectors feature sectors on one side and rings on the other. The objective is to determine the gain for each ring and sector individually.

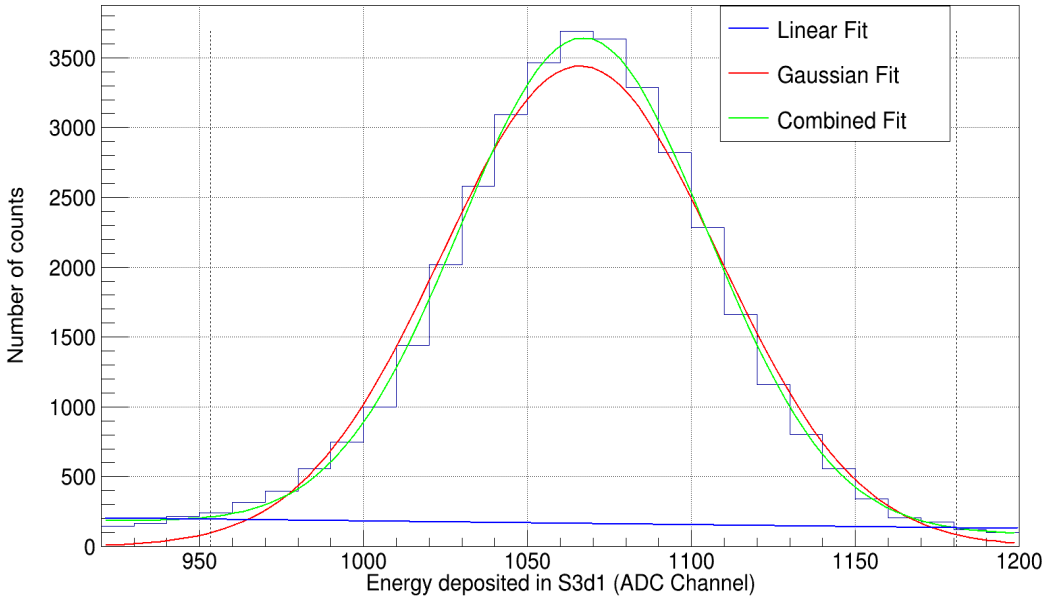

Figure 3.3: The ^{8}He peak in the ADC spectrum for the first ring of the S3d1 detector fitted with a Gaussian + Linear function.

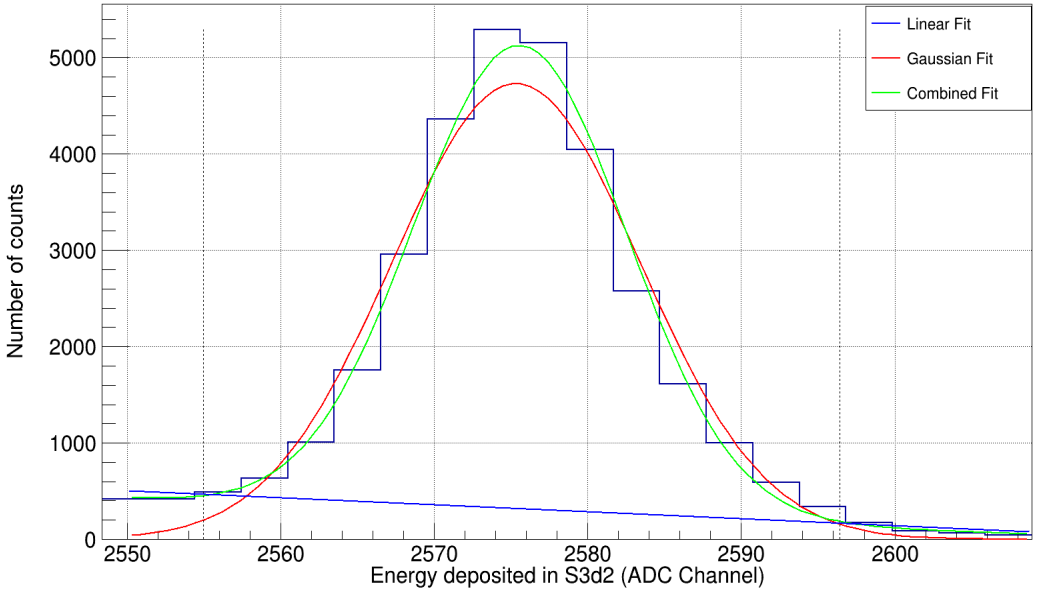

Figure 3.4: The ^{8}He peak in the ADC spectrum for the first ring of the S3d2 detector fitted with a Gaussian function + Linear function.

For each of these segments, the ADC spectrum exhibits a peak as shown in Figure 3.3 and 3.4. Even though gate was applied on the elastically scattered ^{8}He events, still there was some background and hence spectrum was fitted using Gaussian + Linear function. By fitting a Gaussian function to the peak, the corresponding channel number defining the peak can be obtained.

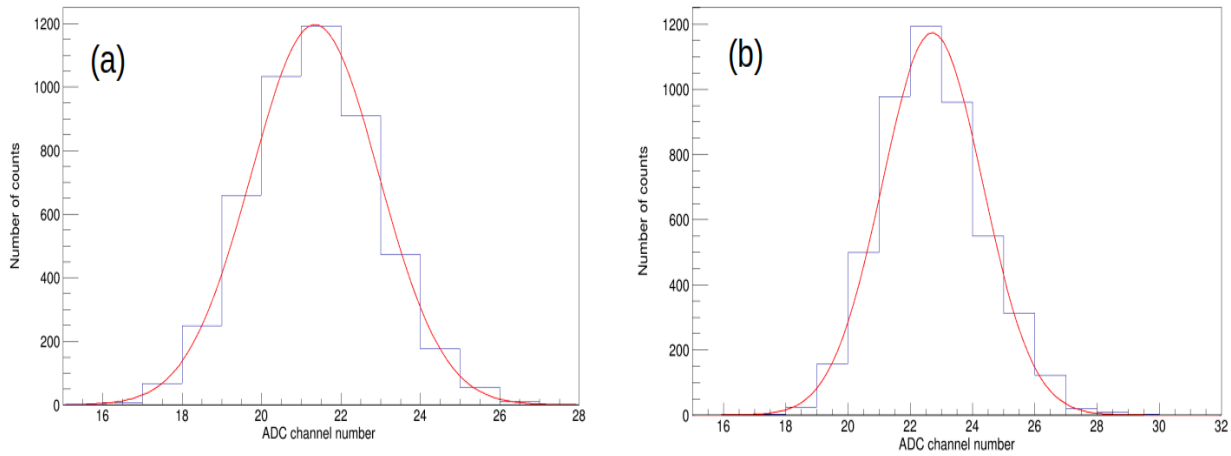

Figure 3.5: The pedestal ADC spectrum for the first ring of the (a) S3d1 and the first ring of (b) S3d2 detector fitted with a Gaussian function.

The pedestals were determined using data collected by the detectors in the absence of a beam in Figure 3.5. The energy related to the peak for each ring that is used for this calibration was calculated using the scattering kinematics. Once the S3 detector is calibrated, it can be utilized to determine the thickness of a solid deuteron target. Figure 3.6 and 3.7 shows calibrated energy vs scattering angle for the elastically scattered ^{8}He with the Ag foil for S3d1 and S3d2 respectively.

3.2.2 Determining the Target Thickness

This section will cover the technique employed to determine the thickness of the solid D_2 target. As noted in the previous chapter, the D_2 target is deposited onto the Ag foil, and knowledge of the

target thickness is necessary to calibrate the CsI(Tl) detector, which will be explained in the next section.

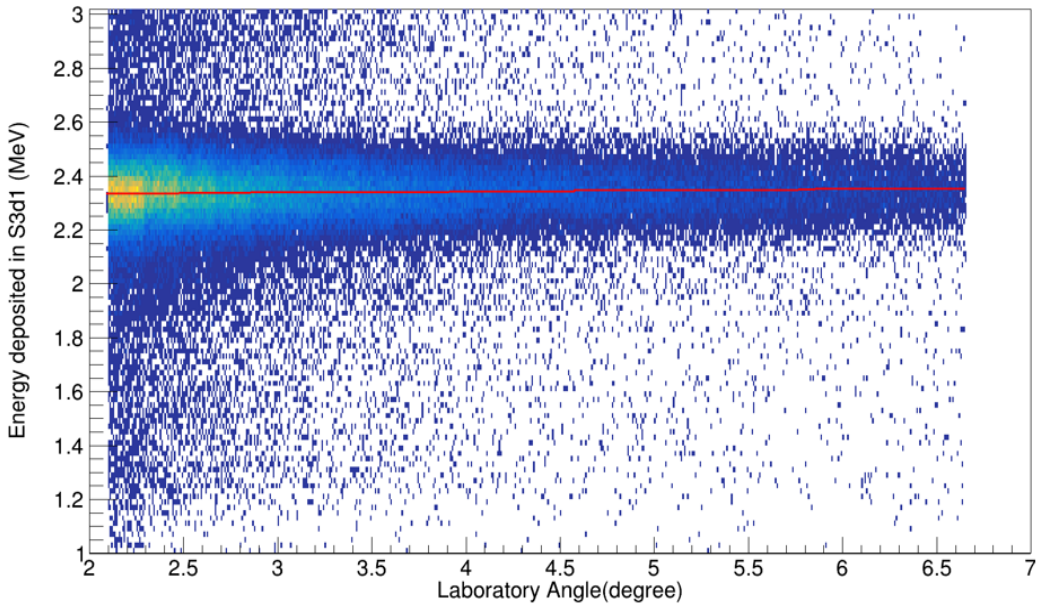

Figure 3.6: Calibrated energy vs. scattering angle for S3d1 detector.

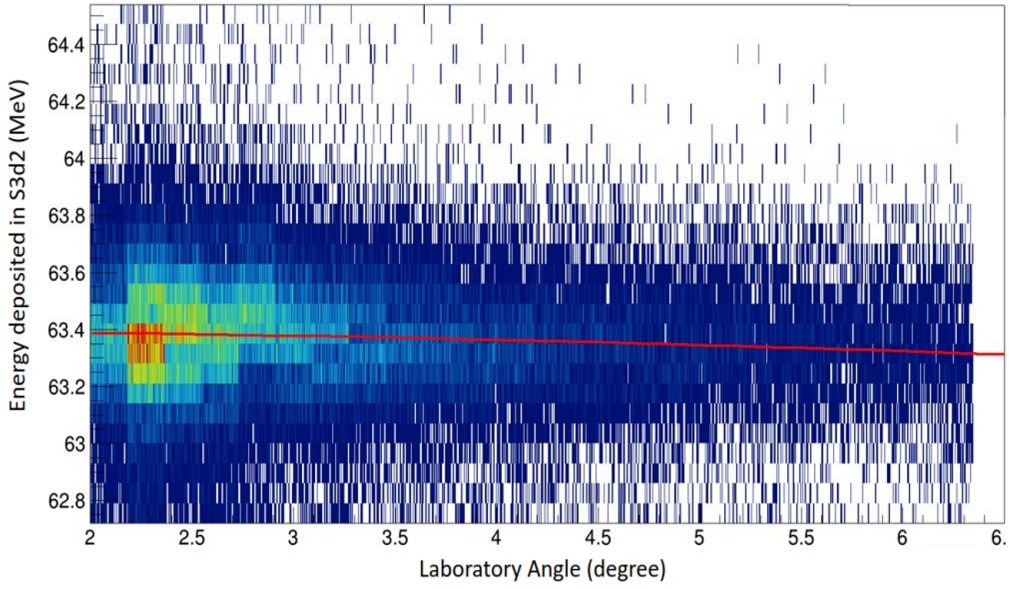

Figure 3.7: Calibrated energy vs. scattering angle for S3d2 detector.

To determine the target thickness, the elastically scattered ^{8}He from the Ag foil detected in the

S3 detectors can be compared with and without the solid D_2 target. By analyzing the difference in the energy of ^{8}He measured with and without the presence of the D_2 target, we can calculate the thickness of the target. Let E_i represent the energy of ^{8}He before the D_2 target, and E_f represent the energy measured after passing through the target and can be seen in Figure 3.8. With this information, the thickness of the solid D_2 target can be determined using the following equation

$$t = \int_{E_i}^{E_f} \frac{1}{S(E)} dE \tag{3.3}$$

Equation 3.3 provides the stopping power, denoted as $S(E)$, of the ^{8}He beam in the D_2 target. To determine E_i and E_f, the energy of the ^{8}He beam must first be reconstructed before it reaches the S3 detectors. As the charged particle traverses through the dead layers and active silicon region of the S3d1 and S3d2 detectors, it loses energy, and the measured energy corresponds to the energy lost in the active silicon. Back-tracing the particle's trajectory enables the reconstruction of the energy of the ^{8}He particle before it enters the S3 detector, as shown in Figure 3.9. The following equation can be utilized to reconstruct the energy of the beam entering the S3 detector:

$$E_{i/f} = E_{\text{S3d2}} + E_{\text{deadlayer2}} + E_{\text{S3d1}} + E_{\text{deadlayer1}} \tag{3.4}$$

where $E_{deadlayer1}$ and $E_{deadlayer2}$ are the energy losses through the dead-layers and E_{S3d1} and E_{S3d2} is the energy deposited in the active silicons. E_i is derived from equation 3.4, using data in the absence of the D_2 target, whereas E_f is derived from data including the presence of the D_2 target.

There was an abnormal increase in the measured target thickness at mid of experiment starting from run number 6752 as shown in Figure 3.10.

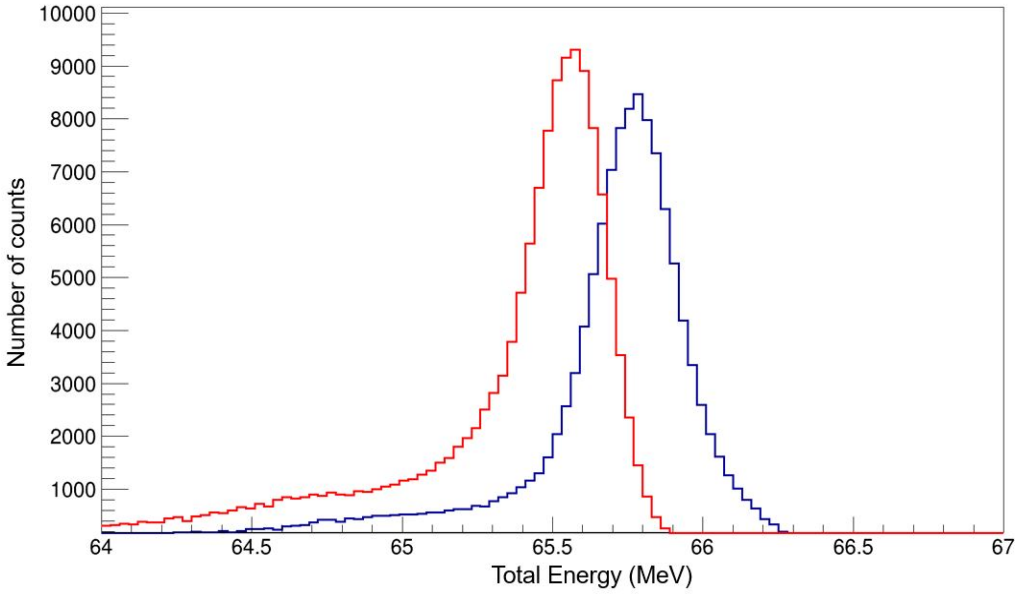

Figure 3.8: The reconstructed energy of the beam for data with D_2 target (red histogram) and for data without D_2 target (blue histogram).

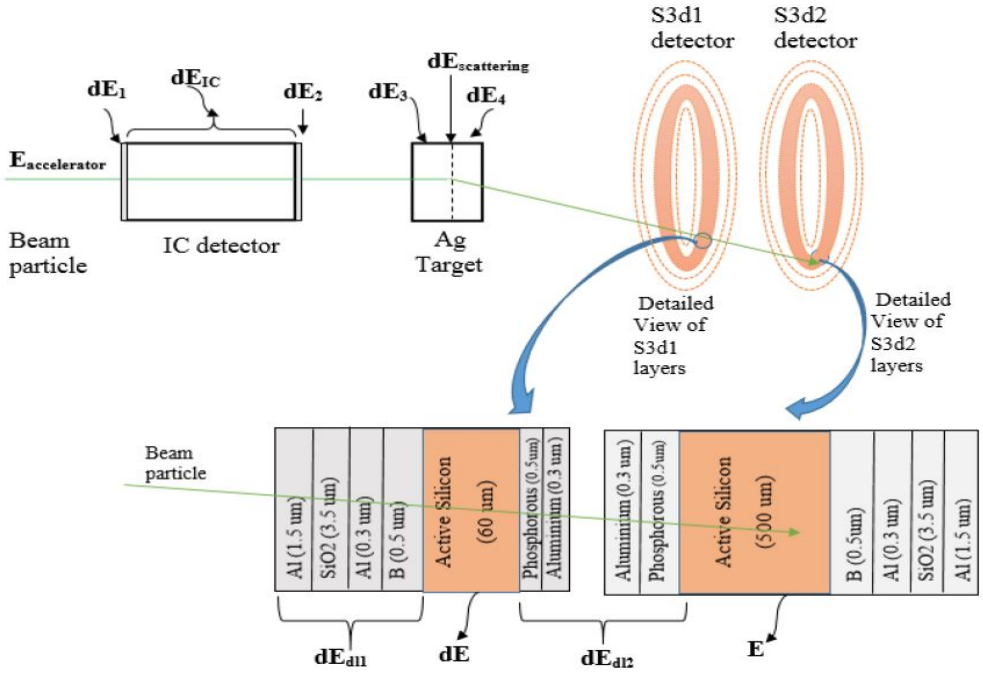

Figure 3.9: Layout of material layers for energy loss calculation in the S3d1 and S3d2 detectors in the absence of solid D_2 target [48].

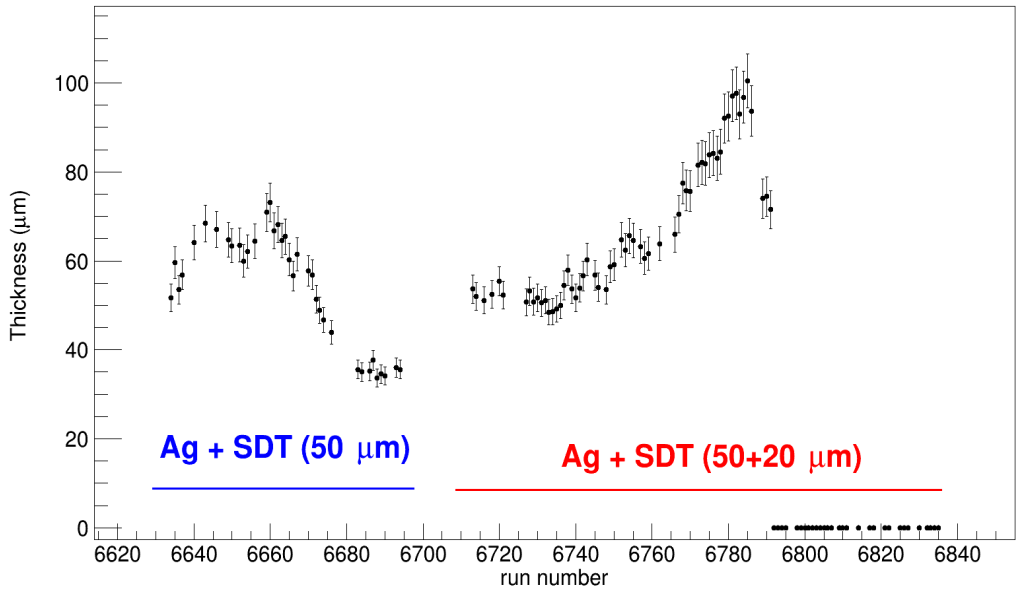

Figure 3.10: The measured target thickness throughout the experiment.

Over time, it was observed that the gain in the S3d2 detector was shifting. The problem was identified by monitoring the peak position of the fixed pulse height peak generated by a pulsar, which ideally should remain constant. A steady decline in the pulsar peak position was noticed as the experiment progressed, with a sharp drop occurring around run 6793. This observation suggests that the gain is shifting, necessitating the correction of the previously calculated gain parameters in the previous section to account for this gain drift. This gain shift led to inaccuracies in the reconstructed energy after passing through the D_2 target, resulting in the measurement of an incorrect target thickness and led to 0 μm thickness after 6793. The gain was corrected using the following relation

$$g_c = g_b \frac{c_b - p_b}{c_c - p_c} \tag{3.5}$$

g_c, c_c, p_c is the corrected gain, pedestal, and pulsar peak position of the base run at the start of the experiment respectively, and g_b, c_b, p_b is the gain, pedestal, and pulsar peak of current

run respectively. The corrected and uncorrected gain can be seen in Figure 3.11. Without gain correction target thickness was found to be 65 $\pm$ 1.4 μm. With the gain correction, the average target thickness was determined based on runs 6633-6692 and 6713-6835 and found to be 55 $\pm$ 0.9 μm shown in Figure 3.12.

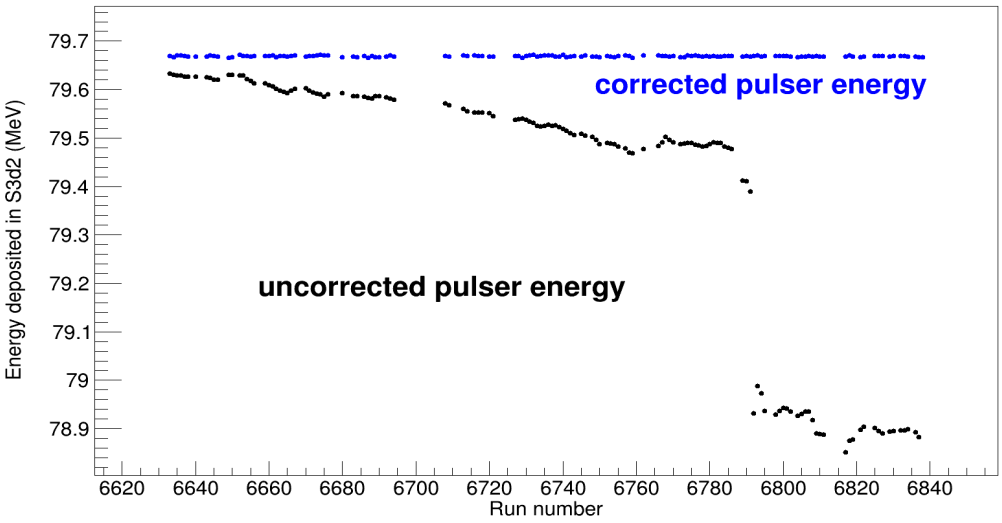

Figure 3.11: The peak position of the pulsar peak for ring 1 of the S3d2 detector without correction (Black) and with gain shift correction (Blue).

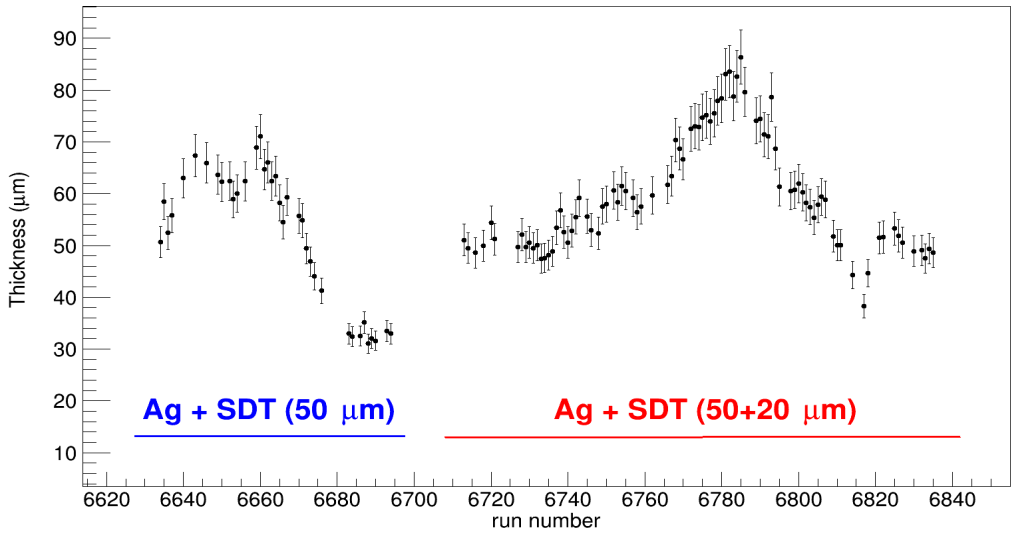

Figure 3.12: The measured target thickness after gain shift correction.

3.2.3 Calibration of the YY1 Detector

To calibrate the YY1 silicon detector, a triple alpha calibration source was used, which comprises of three radioactive isotopes: ^{239}Pu, ^{241}Am, and ^{244}Cm. These isotopes emit alpha particles with most probable energies of 5.155 MeV, 5.486 MeV, and 5.805 MeV, respectively. The source is positioned in front of the YY1 detector using a source holder. After traversing the dead layers of YY1, the alpha particles experience a minimal energy loss of approximately 9 to 11 keV, depositing the remaining energy into the silicon layer. These three peaks can be seen in Figure 3.13 where they are fitted with skewed Gaussian functions.

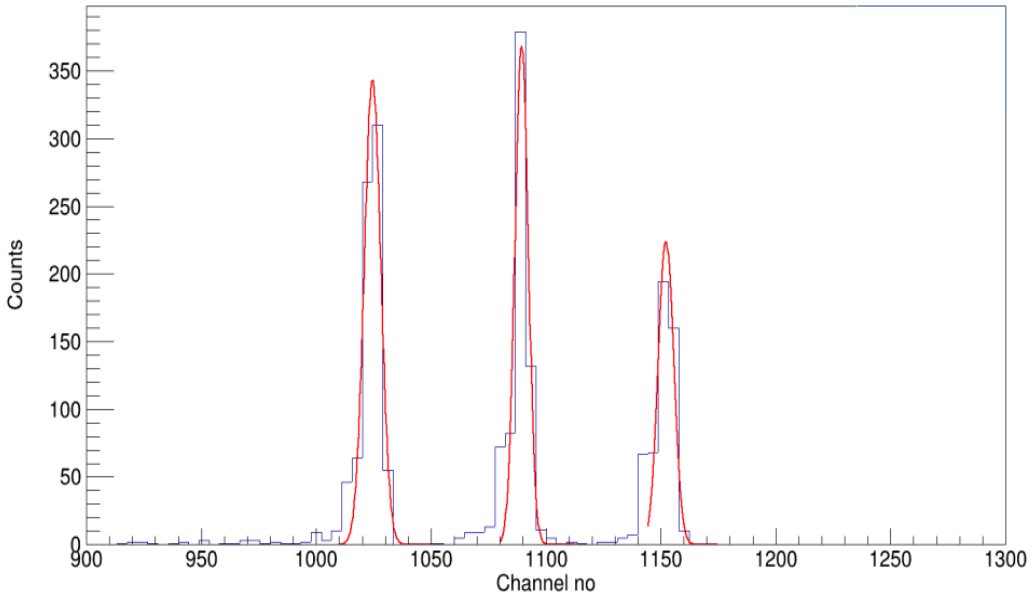

Figure 3.13: YY1 ADC spectrum of ring 2 with alpha source

The mean value of the fitted Gaussian was determined as the position of each peak. By knowing the energies of the alpha particles and the peak positions, a least square fitting process was carried out using equation 3.2 in order to obtain the gain and pedestal values for each detector segment.

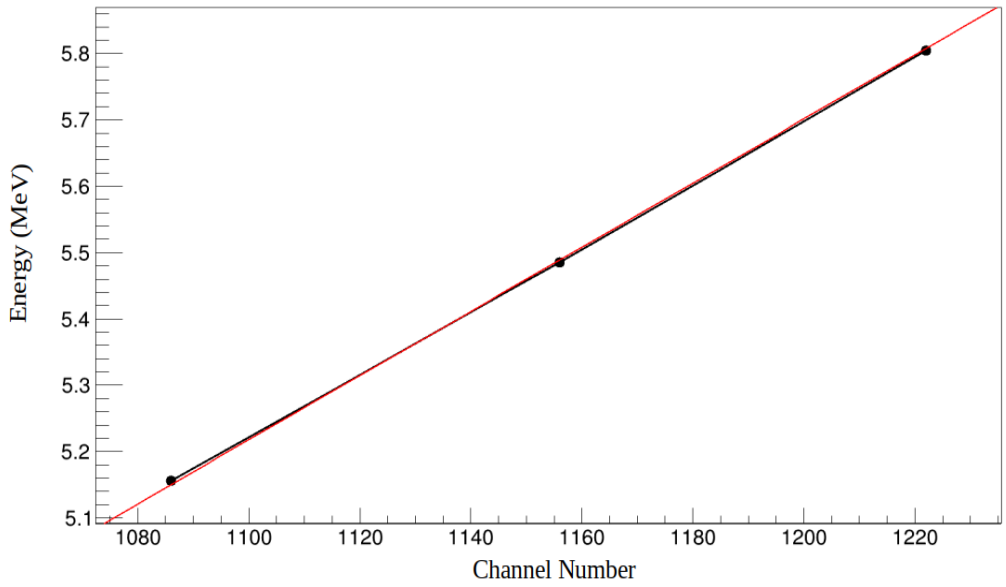

Figure 3.14: Least square fit using the equation 3.2 for YY1 detector

The calibrated YY1 spectrum, depicted in Figure 3.15, displays the outcome of the fitting process.

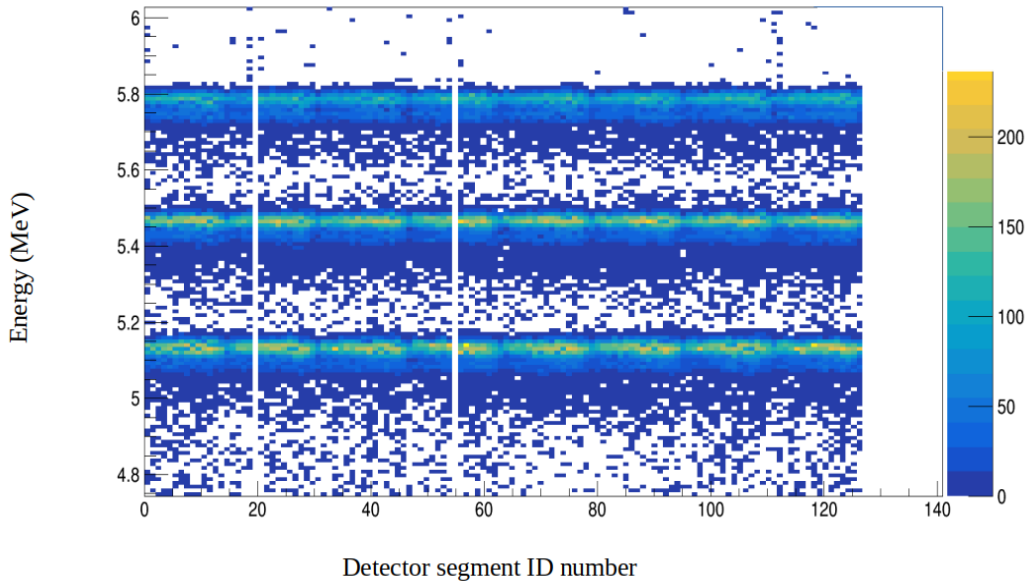

Figure 3.15: Calibrated YY1 spectrum as a function of different detector segments with the triple-alpha source

3.2.4 Calibration of CsI(Tl) Detector

To calibrate the CsI(Tl) we use elastically scattered deuterons from the ^{8}He(d,d) reaction. As we have discussed YY1 and CsI(Tl) acts as $\Delta E - E$ particle identification telescope. Figure 3.16 shows the particle identification correlation. Along the Y axis, we have energy loss (ΔE) in YY1 and along the X axis, we have the remaining total energy (E) deposited in CsI(Tl) by particles. The particle identification plot displays distinct bands representing protons, deuterons, and tritons based on their energy loss due to different velocities. By utilizing these plots, deuterons can be specifically identified and selected inside the red polygon in Figure 3.16, and subsequent data analysis will be done using this gate. To select elastically scattered deuterons, we will look into the CsI(Tl) ADC channel vs the scattered laboratory angle of the deuterons. The upper band selected inside the red polygon are elastically scattered deuterons 3.17.

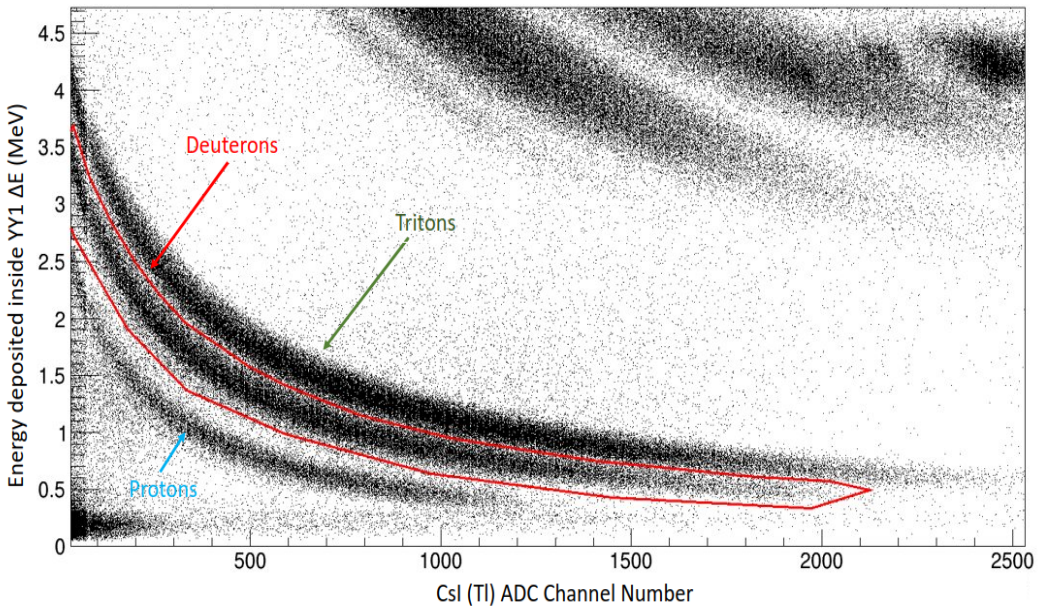

Figure 3.16: The particle identification spectrum for light particles. The red polygon is a selection of the deuteron events

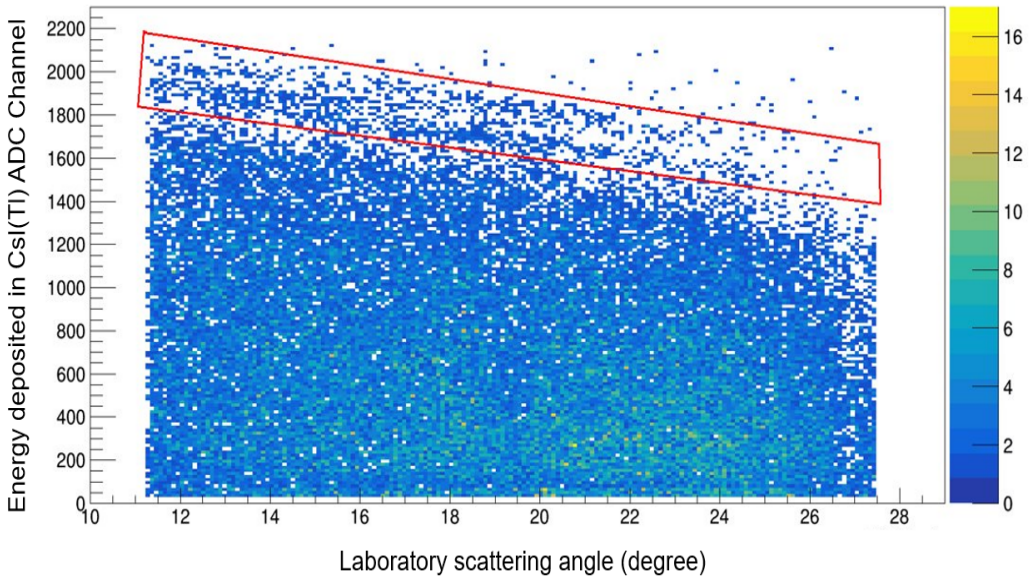

Figure 3.17: Selection of elastic deuterons events from ^{8}He + d scattering using CsI(Tl) detector.

After isolating the elastic deuterons, the next step is to determine the energy they deposit in the CsI(TI) detector. Since scattering occurs uniformly randomly within the target, we consider the average of the scattering to be at the middle of the target. The energy loss through the YY1 dead-layers active silicon region and the CsI(TI) dead-layers was taken into account after the deuteron was scattered. Since angles corresponding to the rings of the YY1 are known and CsI(Tl) is placed just behind YY1 so the angle obtained for each YY1 ring coincident with each of the sixteen sectors of the CsI(Tl) detector. Elastically scattered deuterons are selected in the red polygon for the calibration of CsI(Tl) using using ^{8}He(d,d)^{8}He and shown in Figure 3.17 . A group of four angular segments was taken for the calibrations due to low statistics for individual segments. The elastic peak is fitted using the Gaussian function to find the channel number and the pedestal value was found using pedestal runs shown in Figure 3.18.

Equation 3.2 is used to find the gain for each CsI(Tl) sector for all four angular segments. The

calibration CsI(Tl) array energy as a function of the scattering angle determined from the YY1 detector is shown in Figure 3.19.

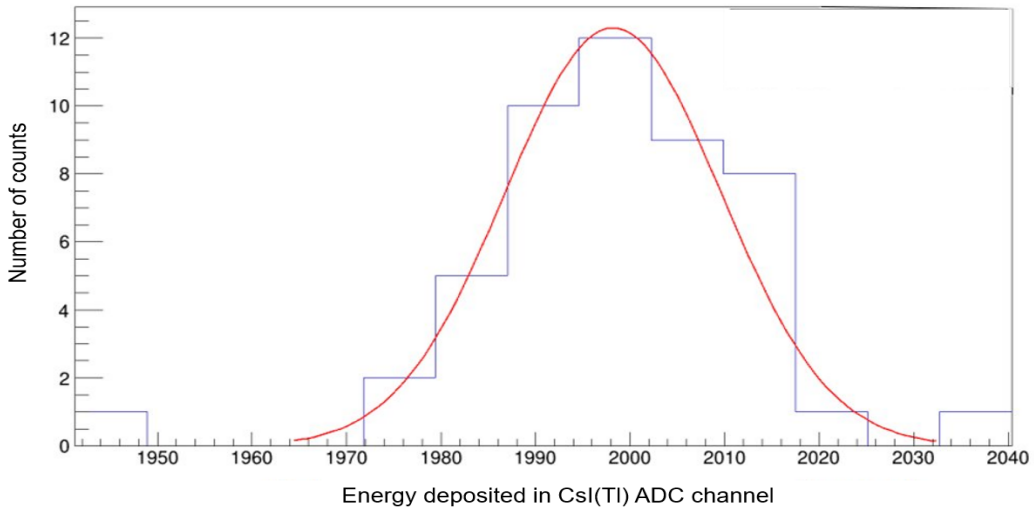

Figure 3.18: The ADC spectrum for ^{8}He(d,d) for CsI(Tl) crystal in coincidence with the first four rings of the matching YY1 sector.

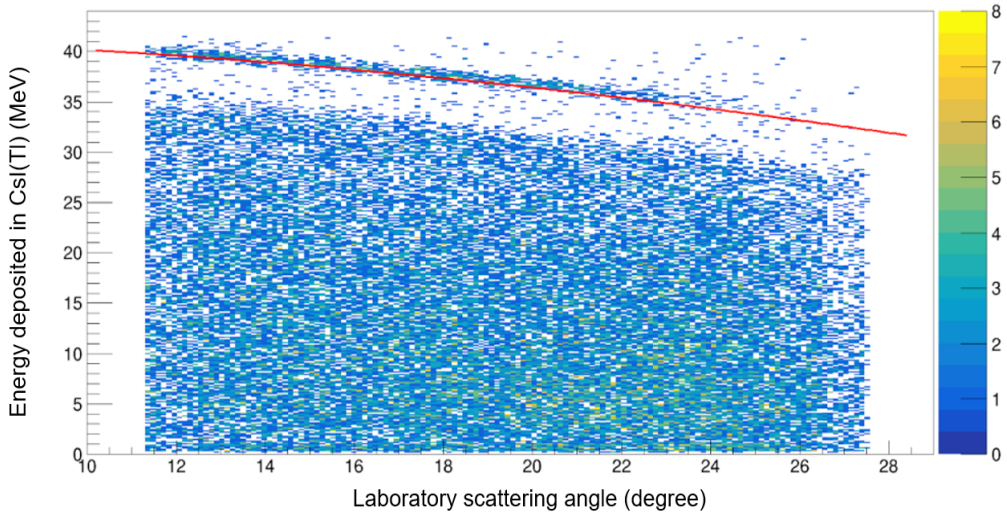

Figure 3.19: Energy deposited by deuterons in CsI(Tl) vs laboratory angle. The red curve shows kinematically calculated energy loss by elastically scattered deuterons inside CsI(Tl).

3.3 Missing Mass Technique

The excitation energy spectrum can be generated by using the missing mass technique. In the missing mass technique, if either one of the scattered particle's energy and angle are measured, one can construct the Q-Value spectrum and hence the excitation energy spectrum. The Q-Value represents the energy that is either released or absorbed in any nuclear reaction. For a nuclear reaction $A + a \rightarrow B + b$, Q-Value can be defined for this reaction by equation 3.6,

$$Q = (m_A + m_a - m_B - m_b)c^2 \tag{3.6}$$

The mass of the beam particle (^{8}He) is given by m_A, the mass of the target particle (deuteron) is given by m_a, the mass of the reacting beam-like particle (^{8}He) is given by m_B, and the mass of the reacting target-like particle (deuteron) is given by m_b. If reaction products (B) are found in an unknown excited state, then their mass differs from their rest mass as a result of the principle of mass-energy equivalence. Using the principle of total momentum conservation and total energy, one can find the particle mass in terms of the variables obtained from the experiment by using equations 3.7 and 3.8

$$E_B = KE_A + m_A c^2 + m_a c^2 - KE_b - m_b c^2 \tag{3.7}$$

$$p_B^2 c^2 = p_A^2 c^2 + p_b^2 c^2 - 2c^2 p_A p_b cos\theta_b \tag{3.8}$$

KE_A represents the kinetic energy of the beam particle, KE_b denotes the kinetic energy of the target-like particle, and p_A and p_b correspond to the momenta of the beam and target-like particle, respectively. θ_b is a scattering angle of particle b. Equation 3.9 establishes a relationship between

the energy of a particle, its mass, and its momentum. By rearranging this equation, as shown in equation 3.10, the mass (m) of an unknown particle can be determined when energy (E) and momentum (p) are known.

$$E^2 = (pc)^2 + (mc^2)^2 \tag{3.9}$$

$$Q = m_A c^2 + m_a c^2 - m_b c^2 - \sqrt{E_B^2 - (p_B c)^2} \tag{3.10}$$

In this case, the particle of unknown mass is the scattered ^{8}He.

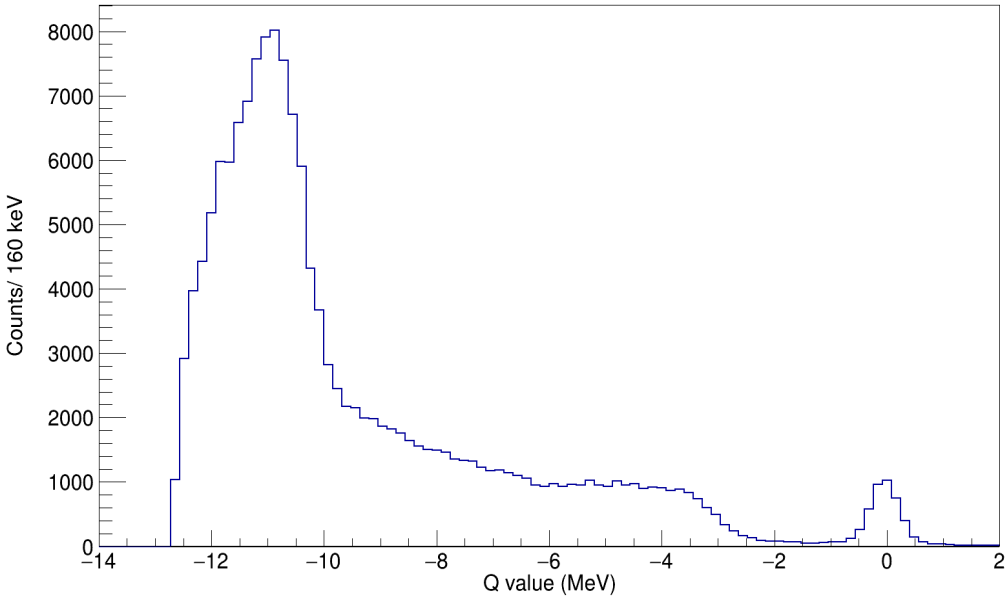

Figure 3.20: Q-spectrum generated using all the deuterons in the particle identification spectrum.

Figure 3.20 shows the Q-Value spectrum for ^{8}He(d,d') with a deuteron target thickness of 55 μm. This spectrum was converted into an excitation spectrum by using

$$E_{exc} = Q_{gs} - Q \tag{3.11}$$

where Q_{gs}= 0 MeV for elastic scattering.

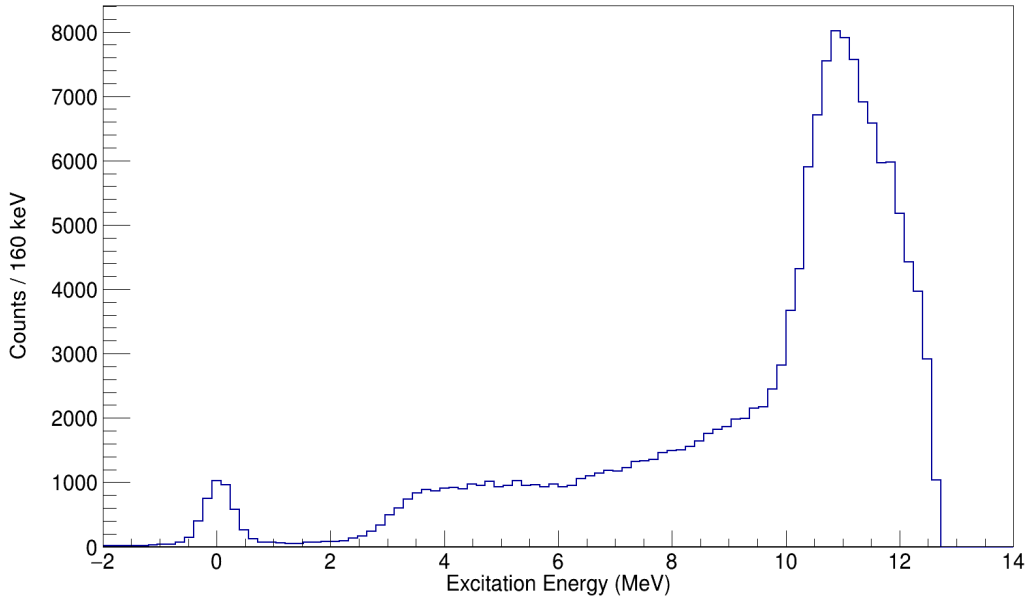

Figure 3.21: Excitation spectrum generated using all the deuterons in the particle identification spectrum.

Figure 3.21 shows the excitation spectrum generated by all the deuterons identified in Figure 3.16. The selected deuterons can have the contribution of deuterons which are coming from the Ag foil via fusion-evaporation reactions and also from ^{8}He + d non-resonant phase space. We can see in Figure 3.21 that only one peak is clearly visible; the ground state of ^{8}He. So our next task is to subtract the background coming from silver foil as well as from non-resonant phase space.

3.4 Background Subtraction

3.4.1 Ag Foil Background

Prior to hitting the solid deuteron target, the ^{8}He beam passes through the Ag foil. Different lighter particles like p, d, t could have been produced as a result of the reactions on the Ag foil (primarily

from fusion-evaporation reactions).

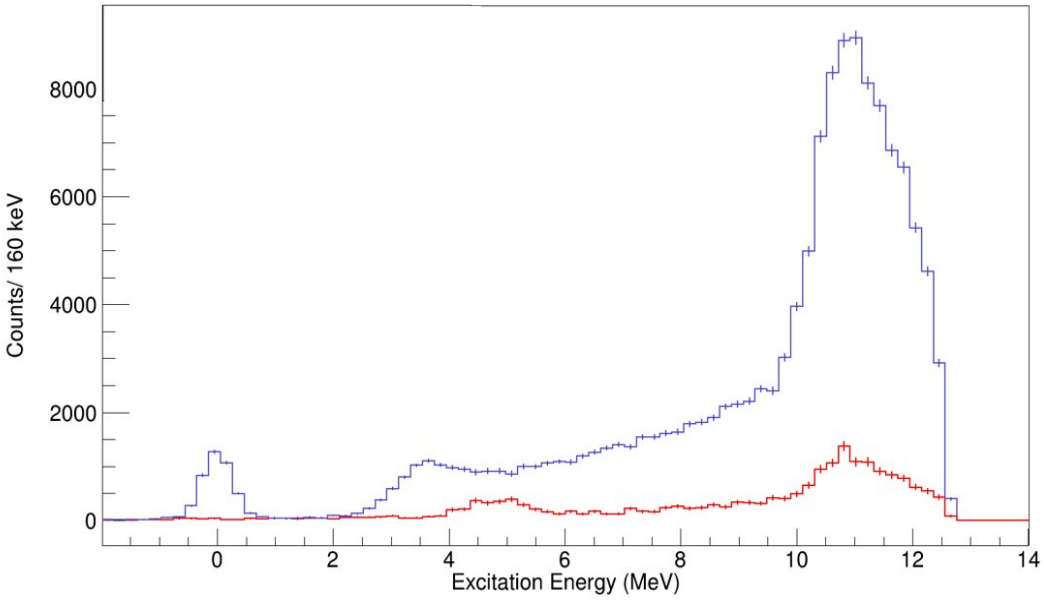

Figure 3.22: Excitation spectrum generated using all the deuterons in the particle identification spectrum. The excitation spectrum with Ag foil is shown in (red) and with D_2 target is shown in blue.

However, these non-target contributions can be measured using data from ^{8}He beam on the Ag foil when no solid D_2 target is present. Figure 3.22 shows the no-target excitation spectrum (red) along with the with-target excitation spectrum (blue). To enable a direct comparison between the two spectra, which have a smaller number of incident particles in the data with no target, the spectrum is scaled using the ratio of the number of incident particles with a target to the number of incident particles with no target.

$$Scaling\ factor = \frac{Number\ of\ incident\ beam\ particles\ for\ D_2\ target\ runs}{Number\ of\ incident\ beam\ particles\ without\ D_2\ target\ runs} \tag{3.12}$$

The normalization factor found for the 55 μm target was 6.31. This normalized background was subtracted from the total excitation spectrum.

3.4.2 Phase Space Contribution

There are other reaction channels that are open at this energy for ^{8}He(d,d'), which can contribute to our excitation spectrum. In this study, these channels are ^{8}He + $d \rightarrow {}^{7}$He + d + n three body reaction, ^{8}He + $d \rightarrow {}^{6}$He + d + n + n four body reaction, ^{8}He + $d \rightarrow {}^{5}$He + d + n + n + n five body reaction and ^{8}He + $d \rightarrow {}^{4}$He + d + n + n + n + n six body reaction. These all are non-resonant reaction channels that will not contribute to the resonant state. The excitation spectrum consists of all these reaction channels and we simulated the excitation spectrum for ^{8}He(d,d') considering the kinematics of the deuterons arising from the different non-resonant channels. The simulation specifically modeled the non-resonant phase space, taking into account the isotropic emission of the products in the center-of-mass frame. The simulation employed the utility class 'TGenPhaseSpace' within ROOT, a data analysis framework developed by CERN [49, 50]. This class facilitated the simulation of the kinematics of the process by generating events with an n-body final state. It enabled the simulation of the decay of a particle, defined by its Lorentz four-momentum, into n-bodies. The simulations also consider experimental conditions, such as the beam energy, energy loss due to particle-material interactions, and the geometry of the detector. Figure 3.23 shows the contributions of the non-resonant channels individually for the ^{8}He excitation spectrum.

To normalize the background from non-resonant phase space, the total excitation spectrum is fitted using total fit function which includes contributions from non-resonant reaction channels (silver foil background + phase space) and an energy-dependent Voigt function which will be discussed in detail in subsection 3.5.4. The scaling parameters were free and independent for all the phase space background channels. The total scaled background is expressed as the sum of contributions from individual non-resonant background channels and each K^{BKG} term scales the

contribution of a specific non-resonant background channel.

- Total scaled background = $K^{BKG1}\times$ BKG1 + $K^{BKG2}\times$ BKG2 + ...

These contributions were scaled to the total excitation spectrum through χ^2 minimization. We separate the contribution of non-resonant phase space (in Cyan) from the measured excitation spectrum (in blue) in Fig 3.24. By subtracting the phase space excitation spectrum, we obtain the excitation spectrum for our specific reaction of interest i.e. ^{8}He(d,d'). The excitation spectrum from the six-body reaction has larger contributions at the higher excitation energy regions but for three-body and four-body reactions, the non-resonant background is present in the excitation energy region around 3.6 MeV.

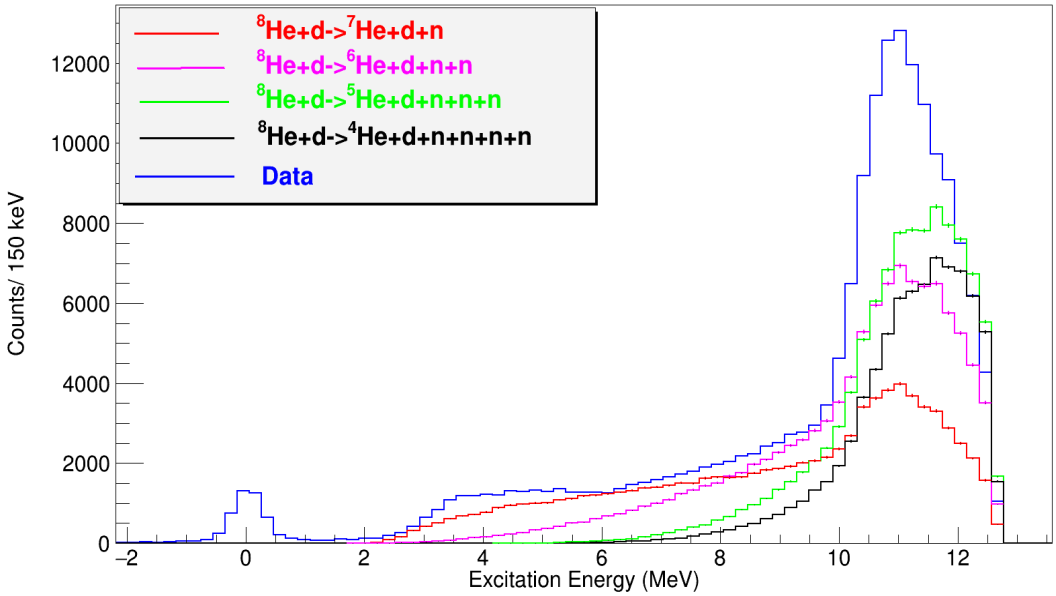

Figure 3.23: Excitation spectrum for ^{8}He with the Ag foil background substracted. The blue histogram is the measured spectrum, and the red histogram is the non-resonant background with the ^{8}He + d $\rightarrow$ ^{7}He+ d + n channel contribution, pink histogram is ^{8}He + d $\rightarrow$ ^{6}He + d + n + n contribution, the green histogram is ^{8}He + d $\rightarrow$ ^{5}He + d + n + n + n contribution, and black histogram is ^{8}He + d $\rightarrow$ ^{4}He + d + n + n + n + n contribution

3.5 Measurement of Differential Cross Section

The final goal of this study is to extract the differential cross sections $d\sigma/d\Omega$ for the ground state and the observed resonance state at 3.57 MeV. The differential cross-section is defined as:

$$\frac{d\sigma}{d\Omega} = \left[\frac{N^s}{N^{in}}\right] \times \left[\frac{M_t}{N_A} \times \frac{1}{\rho T} \times \frac{1}{d\Omega}\right] \tag{3.13}$$

At each instant, the target thickness 'T' is known, while the molar mass 'M_t', density 'ρ', and Avogadro's number 'N_A' remain constant for the solid D_2 target. 'N^s' represents the number of scattered particles, 'N^{in}' represents the number of incident particles, and '$d\Omega$' represents the solid angle.

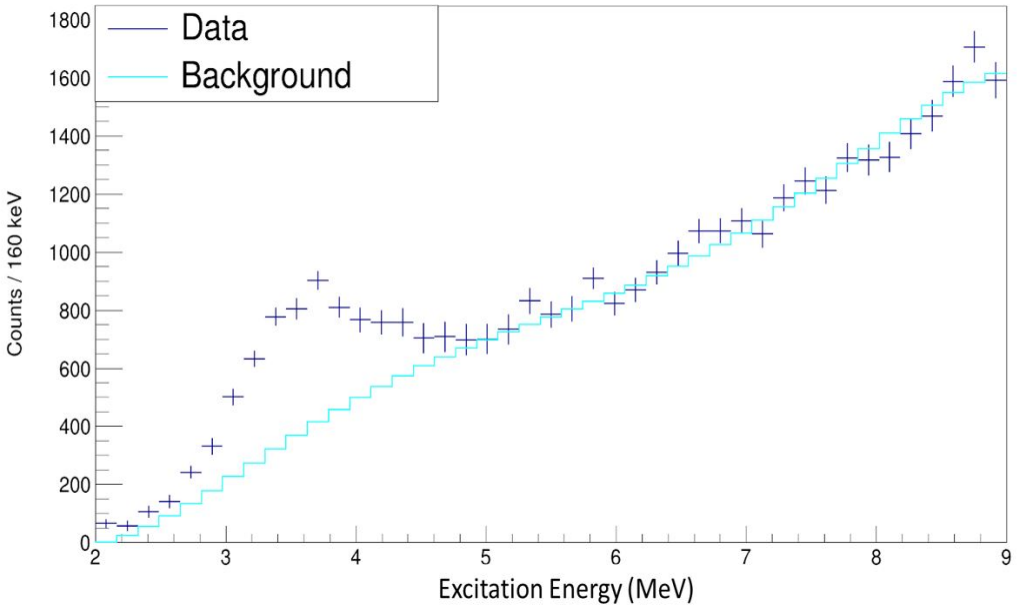

Figure 3.24: The normalized sum of all non-resonant phase space channels (Cyan) and the measured excitation spectrum (blue).

3.5.1 Incident Beam Counting

Beam particles are identified by the IC and after the identification, the next task is to count the number of incident ^{8}He beam particles. As discussed in section 3.1, even though there was the presence of only one Gaussian peak indicating that ^{8}He is uncontaminated, still we have to put a selection gate on the ADC spectrum containing ^{8}He to eliminate any possibility of electronic noise at lower channels. The number of ^{8}He particles in the incident beam that passes through the IC is recorded in the IC scaler. We have measured the number of incident ^{8}He particles for each data run separately. With the help of the data acquisition live-time (DAQ) correction, we were able to determine the ratio of the integral of ^{8}He particles to the total integral in the IC ADC spectrum. The data acquisition live-time (τ) is a crucial component that must be taken into account when counting incident flux because it takes a certain time to process and store each event that occurs on the YY1 or S3d1 detectors. If Any hits in the YY1 or S3d1 were in the trigger, the data acquisition system cannot process and store all of these events. The storage of events can only take place when there is an accepted trigger, thus we need to correct the incident ^{8}He beam particle by the same ratio as seen in Figure 3.25. The DAQ live-time is given as:

$$\tau = \frac{Total\ accepted\ trigger}{Total\ free\ trigger} \tag{3.14}$$

Thus, the effective number of the incident ^{8}He particles (N_i^{8He}) in the i^{th} run can be written as

$$N_i^{8He} = (IC\ scaler\ counts\ in\ the\ i^{th}\ run) \times \tau_i \times \frac{N_i^{\mathrm{ADC}^{(8He\mathrm{gate})}}}{N_i^{\mathrm{ADC}^{(total)}}} \tag{3.15}$$

τ_i is DAQ live-time for the i^{th} data run, $N_i^{\mathrm{ADC}^{(8He\mathrm{gate})}}$ is the number of ^{8}He particles in the

IC ADC spectrum for the i^{th} run, and $N_i^{ADC(total)}$ is the total number of particles in the IC ADC spectrum for the i^{th} data run. The quantity N^{in} in equation 3.13 can be expressed as

$$N^{in} = \sum_i N_i^{8He} \tag{3.16}$$

Target thickness was not constant over the period of time which was measured for each run. To calculate the differential cross section systematically, we have to modify the term "$N^{in} * T$" in equation 3.13 in the following manner

$$N^{in} \times T = N_1^{8He} \times t_1 + N_2^{8He} \times t_2 + ... \tag{3.17}$$

where t_i is the solid D_2 target thickness for i^{th} data run. The DAQ live-time and N^{in} for each data run is shown in Figure 3.25 and 3.26 respectively.

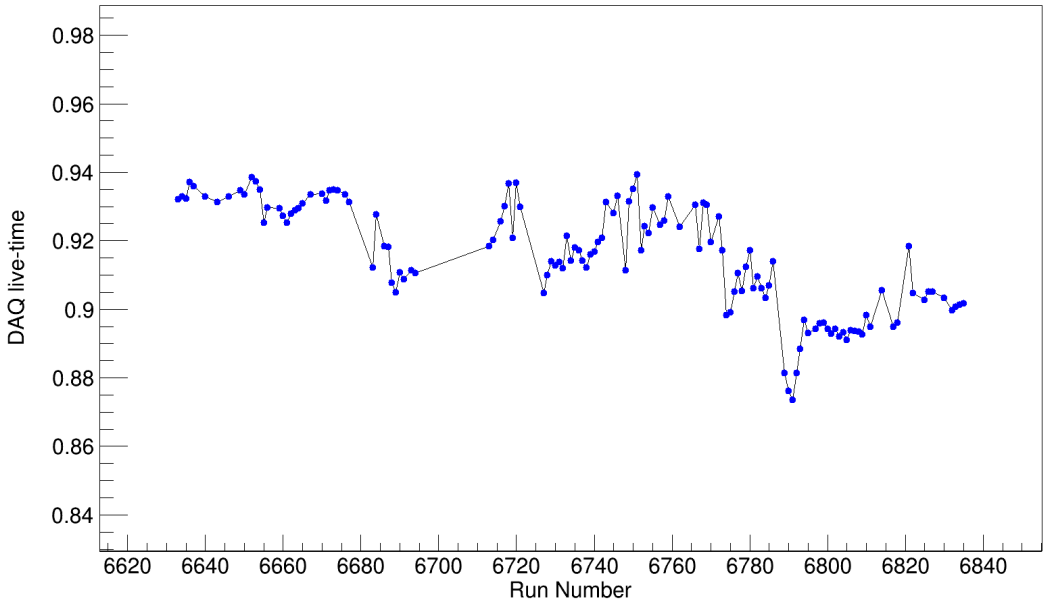

Figure 3.25: DAQ live-time for all data runs.

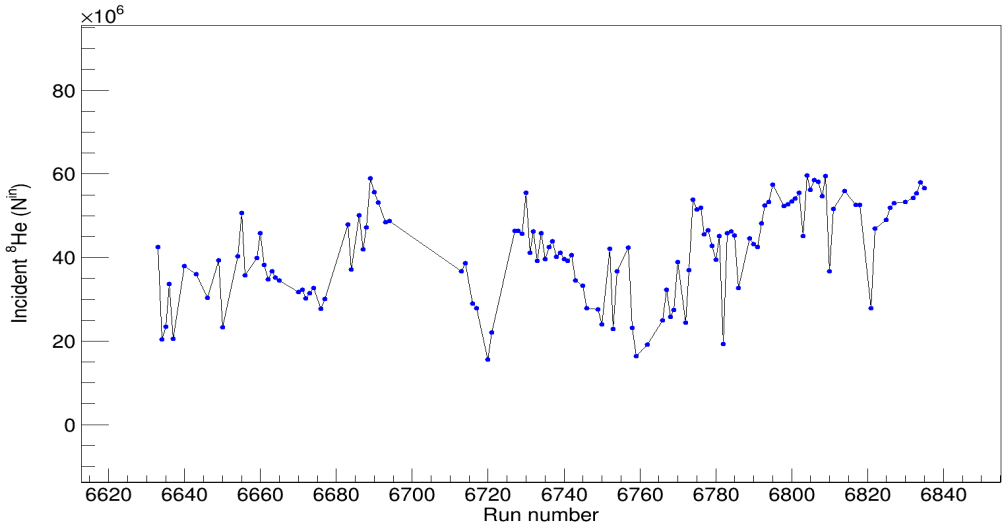

Figure 3.26: N^{in} for all data runs.

3.5.2 Differential cross section for ^{8}He ground state

In order to get the differential cross-section for each scattering angle for the ground state, we measure the scattering flux, i.e. the number of deuterons produced from the elastic channel for a given angular bin (each ring) of the YY1 detector. To count the number of scattered deuterons from elastic scattering, we have generated the excitation spectra for each ring from 1 to 12 and for rings 13 to 16 together, due to low statistics. This spectrum is then fitted with the sum of a linear and Gaussian function because the area under the peak also has a contribution from the Ag-foil background. The resolution corresponding to the ground state was obtained using simulations that were performed by taking into account the same experimental conditions and parameters. The background under the peak is linear throughout. The fitting function can be written as

$$f(x) = \left[A \times e^{\left(-0.5 \times \left[\frac{x-\mu}{\sigma}\right]^2\right)}\right] + [c_0 + c_1 \times x] \tag{3.18}$$

where A, μ, and σ are the amplitude, peak position, and standard deviation of the Gaussian peak, respectively. c_0 and c_1 are the parameters of the linear background function. In the spectrum (Figure 3.27), the total counts (N^{total}) were obtained from the integral under the $\pm$ 3σ region of the peak(black) and the integral of background counts(N^{back}) are estimated under linear function within the 3σ range. The number of scattered deuterons is given by

$$N_d^{sc} = N^{total} - N^{back} \tag{3.19}$$

The quantity N_d^{sc} has been used as N^s in equation 3.13 to evaluate the differential cross-section. Similarly, the same procedure was repeated for the other rings. The solid angle for each angular bin (one ring of the YY1 detector) can be written as

$$d\Omega = 2\pi \times sin(\theta_{lab}) \times d\theta_{lab} \tag{3.20}$$

where

$$\theta_{lab} = \frac{\theta_{lab}^{max} + \theta_{lab}^{min}}{2} \tag{3.21}$$

and

$$d\theta_{lab} = \theta_{lab}^{max} - \theta_{lab}^{min} \tag{3.22}$$

where θ_{lab}^{max} and θ_{lab}^{min} are the maximum and minimum laboratory angles subtended by the selected ring and θ_{lab} is an average angle of the given ring of the YY1 detector. The factor 2π in equation 3.20 comes from the integration over the azimuthal angle. The detection efficiency (E) of the YY1 detector varied across different rings due to their different azimuthal angle coverage due gaps between the sectors. This gap is same for inner thirteen rings and different for rings 14,15 and 16. We also need to take detection efficiency (E) into account, so that an effective solid angle will be

$$d\Omega_{eff} = 2\pi \times E \times sin(\theta_{lab}) d\theta_{lab} \tag{3.23}$$

The total detection efficiency of the detector can be seen in Figure 3.28.

Now we have knowledge of both unknown quantities N_d^{sc} and $d\Omega_{eff}$, the differential cross-section can be written as

$$\frac{d\sigma}{d\Omega} = \left[\frac{N_d^{sc}}{\sum_i N_i^{8He} \times t_i}\right] \times \left[\frac{M_t}{2N_A} \times \frac{1}{\rho} \times \frac{1}{d\Omega_{eff}}\right] \times 10^{31} mb/sr \tag{3.24}$$

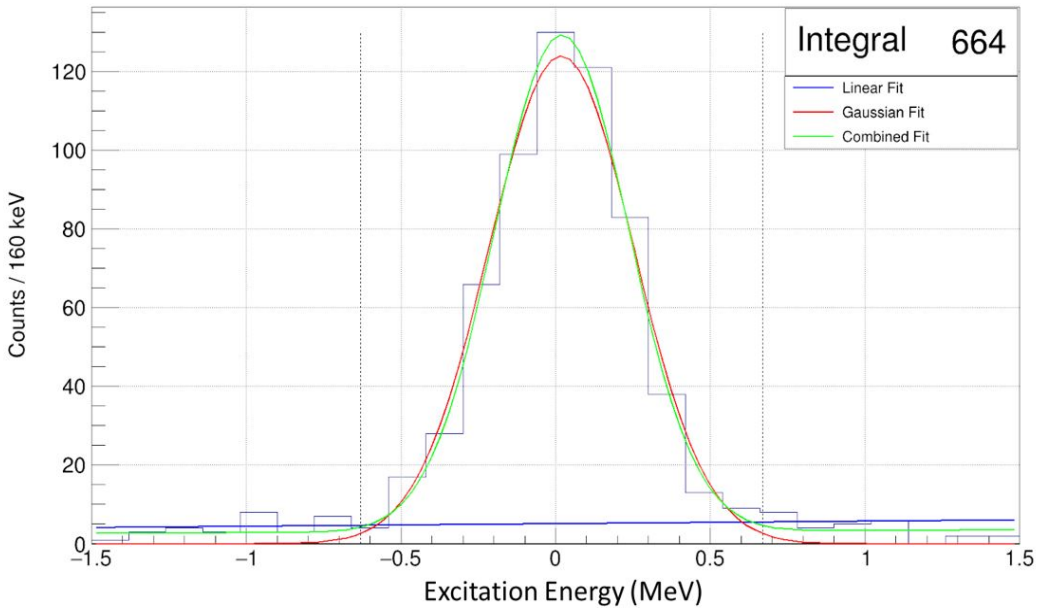

Figure 3.27: Q-value spectrum for ^{8}He$(d,d)^8$He reaction for the rings 7 of the YY1. The two vertical dashed lines show the 3σ range around the peak position.

where

- M_t = 2 × 2.014 g/mol (Molar mass of D_2)

- $\rho = 0.201 \times 10^6$ g/m^3 (Density of solid D_2 target)
- $N_A = 6.023 \times 10^{23}$ (Avogadro's number)

In our experiment, we used the S3 detector to identify the ^{8}He nuclei that were elastically scattered. Therefore, using the ^{8}He, we can also determine the elastic peak and the elastic cross section. We measure the scattering flux, i.e. the number of ^{8}He produced for a given angular bin (2 rings) of the S3 detector. We have generated the excitation spectrum of ^{8}He using the missing mass technique but in this case missing mass is deuteron. Excitation spectrum is generated for the set of 2 rings from ring 10 to ring 23, for which the ground state is resolved between ^{8}He$(d,d)^8$He and ^{8}He$(Ag,Ag)^8$He reactions. Figure 3.29 and 3.30 shows the total excitation spectrum for rings 16-17 and 20-21 (in blue) as well as the scaled background from Ag-foil (in red).

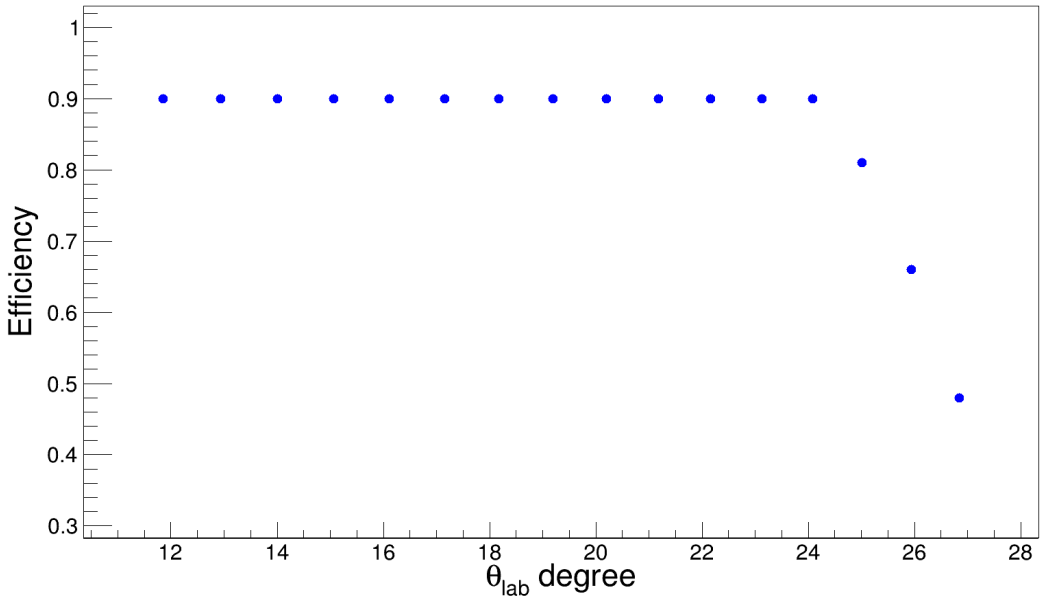

Figure 3.28: Geometric efficiency of the YY1 detector array.

The integral under $\pm 3\sigma$ (for blue histogram) gives total counts (N^{total}) and the integral under red histogram gives background counts (N^{back}). A similar process is used to extract the number of

scattered counts ($N^{sc}_{^8He}$) for other sets of rings.

3.5.3 Uncertainty in the Measurement of Differential Cross Section

We utilized various factors to determine the level of uncertainty. These factors include the uncertainty in the count of scattered particles, the uncertainty in detection efficiency, and the uncertainty in determining the thickness of the target. The uncertainty in the scattered particles will have contribution coming from the silver foil. The background data for the silver foil is scaled using IC scalar values with and without target runs as discussed in eq. 3.12 of section 3.4.1 and this scaling factor (S) must also be included inside the propagation of error. $N_i^{background}$ is silver background without scaling. The uncertainty in the thickness of the solid deuteron target is estimated to be 5% which accounts for the uncertainty arising from the stopping power tables. The uncertainty arising from non-resonant background for ^{8}He(d,d') will be discussed in subsection 3.5.4.

The uncertainty in the detection efficiency is assumed to be 5%, due to any uncertainties related to simulating the geometry and considering the high sensitivity of detection efficiency to the position of the detector. These two uncertainties constitute the systematic uncertainty for the differential cross sections.

$$\Delta\frac{d\sigma}{d\Omega} = \frac{d\sigma}{d\Omega} \times \sqrt{\left(\frac{\sigma^2_{N_{sc}}}{N^2_{sc}}\right) + \left(\frac{\sum_i \sigma^2_{ti} \times (N_i^{8He})^2}{\left(\sum_i N_i^{8He} \times t_i\right)^2}\right) + \left(\frac{\sigma^2_{Eff}}{E^2}\right)} \tag{3.25}$$

where,

- $N_{sc} = N_i^{total} - S \times N_i^{background}$
- $\sigma^2_{N_{sc}} = N_i^{total} + S^2 \times N_i^{background}$

- $\sigma_{t_i}^2 = \frac{25}{10000} \times t_i^2$
- $\sigma_{Eff}^2 = \frac{25}{10000} \times E^2$

The extracted differential cross section measured in the laboratory frame for ground state is shown in Figure 3.31.

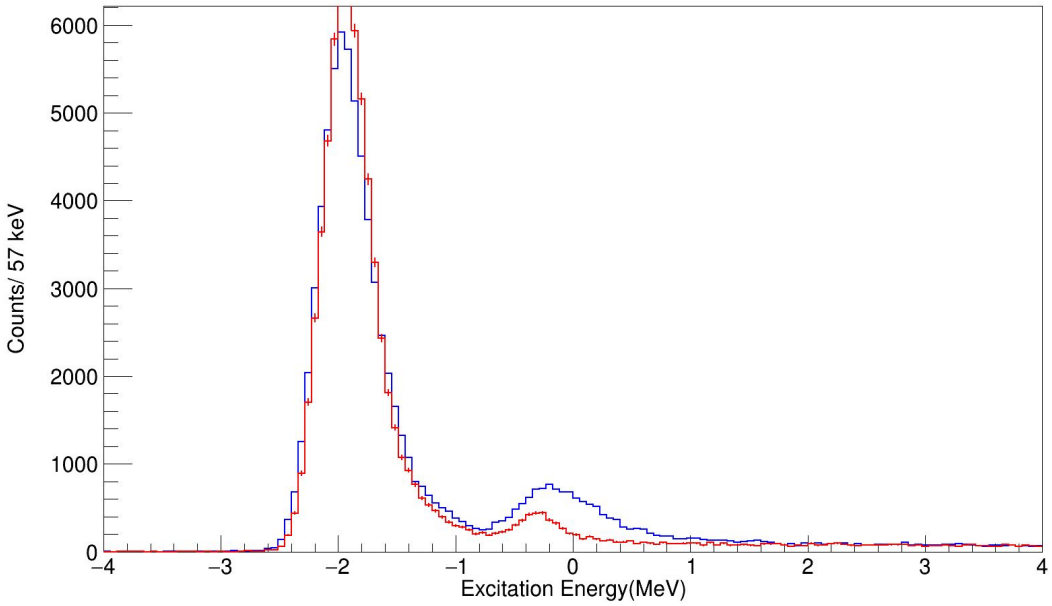

Figure 3.29: Total excitation spectrum for rings 16 and 17 (in blue) and scaled background from Ag-foil (in red).

The differential cross section measured in the laboratory frame can be converted into a center-of-mass (CM) frame by finding the Jacobian of the transformation ($J_{lab \to cm}$) from the laboratory frame to the CM frame as shown in Figure 3.32. Thus, the differential cross section in the CM frame can be written as:

$$\frac{d\sigma}{d\Omega_{cm}} = \frac{d\sigma}{d\Omega_{lab}} \times J_{lab \to cm} \tag{3.26}$$

where

$$J_{lab\to cm} = \frac{d\Omega_{lab}}{d\Omega_{cm}} = \left[\frac{sin(\theta_{lab}) \times d\theta_{lab}}{sin(\theta_{cm}) \times d\theta_{cm}}\right] \tag{3.27}$$

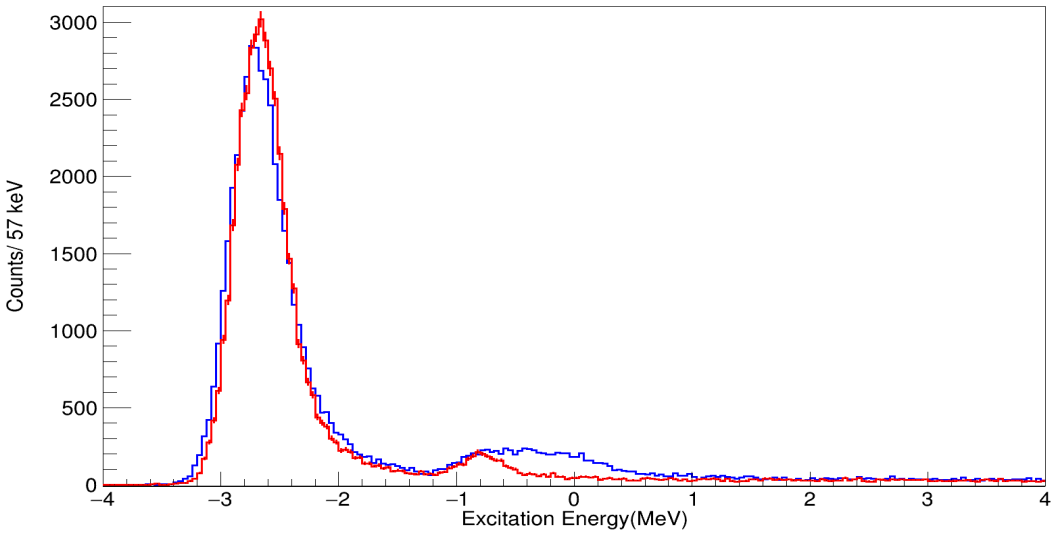

Figure 3.30: Total excitation spectrum for rings 20 and 21 (in blue) and scaled background from Ag-foil (in red).

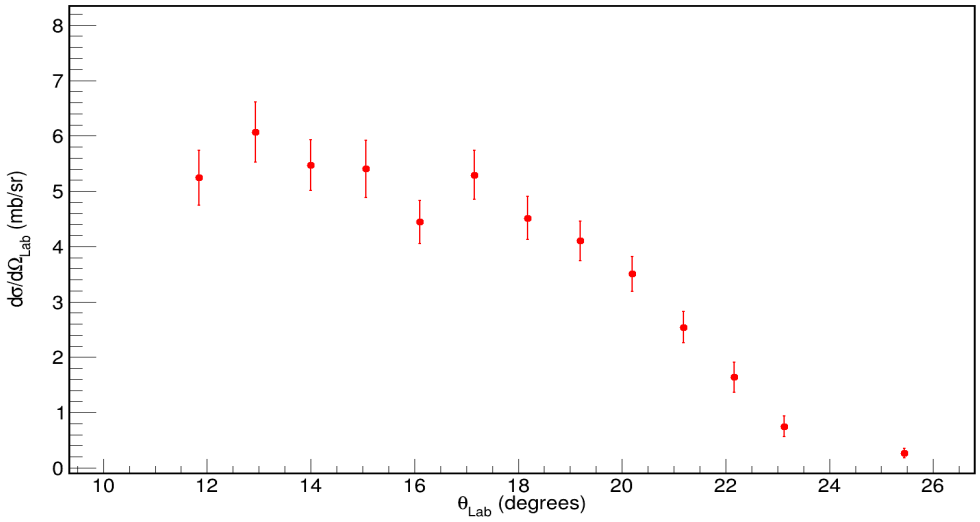

Figure 3.31: Differential cross section for ^{8}He$(d,d)^{8}$He(g.s.) in laboratory frame from observed deuterons.

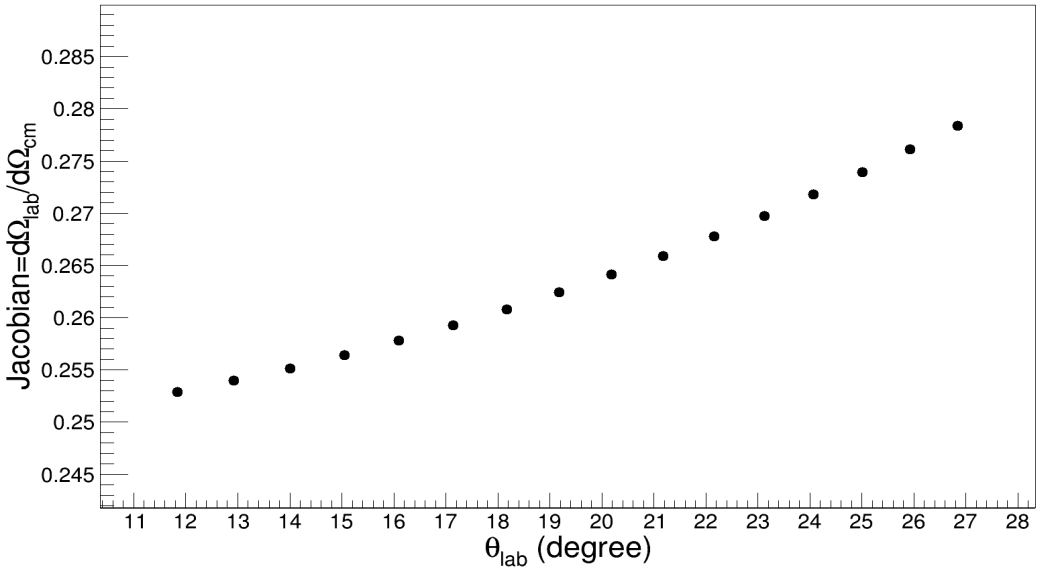

Figure 3.32: The Jacobian of the transformation from the laboratory frame to the center-of-mass frame.

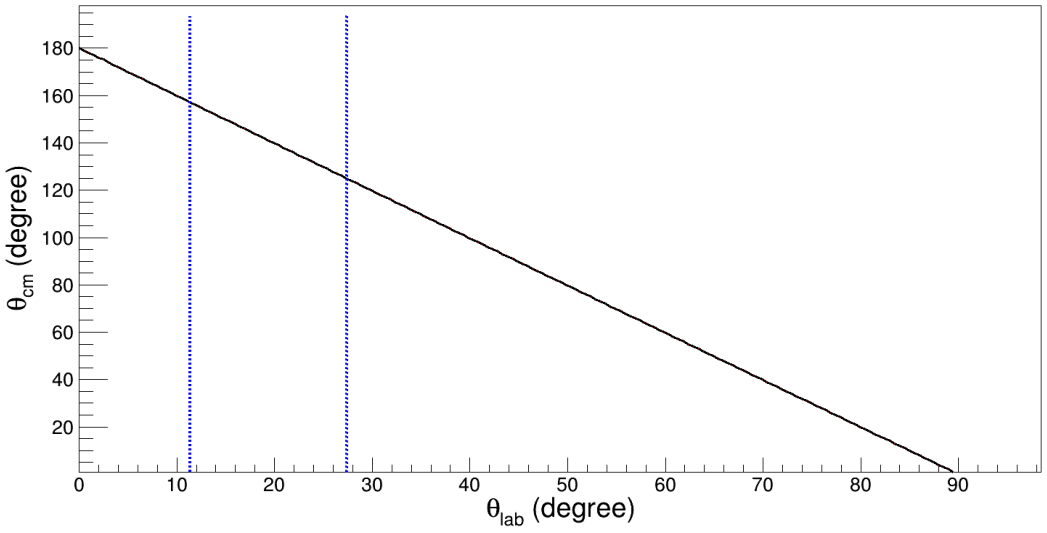

Figure 3.33: The plot of center-of-mass scattering angle versus scattering angle in the laboratory frame.

The same methodology that was used for the light particle detector was utilized to extract the differential cross section for the S3 detector in both the laboratory frame (depicted in Figure 3.35)

and the center-of-mass frame (depicted in Figure 3.36). The differential cross section from both detectors is presented in Figure 3.37 in the center-of-mass frame.

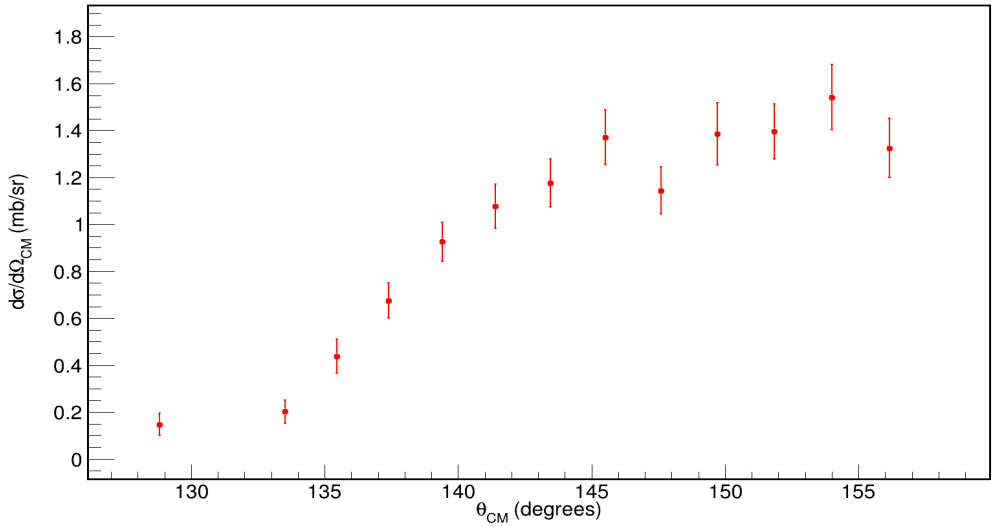

Figure 3.34: Differential cross section for ^{8}He$(d,d)^{8}$He(g.s.) in CM(center of mass) frame from observed deuterons.

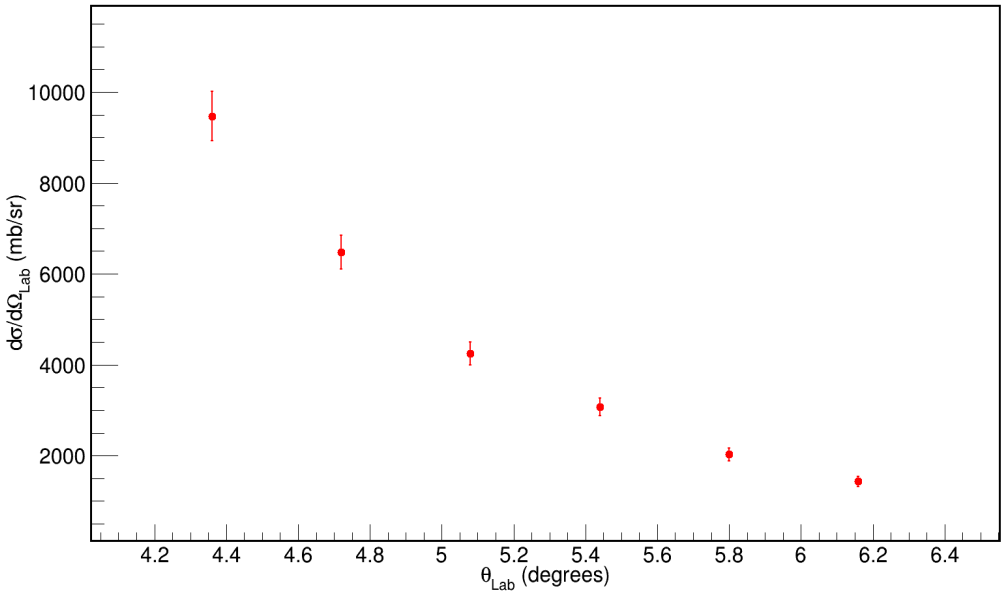

Figure 3.35: Differential cross section for ^{8}He$(d,d)^{8}$He(g.s.) in laboratory frame using S3 detector.

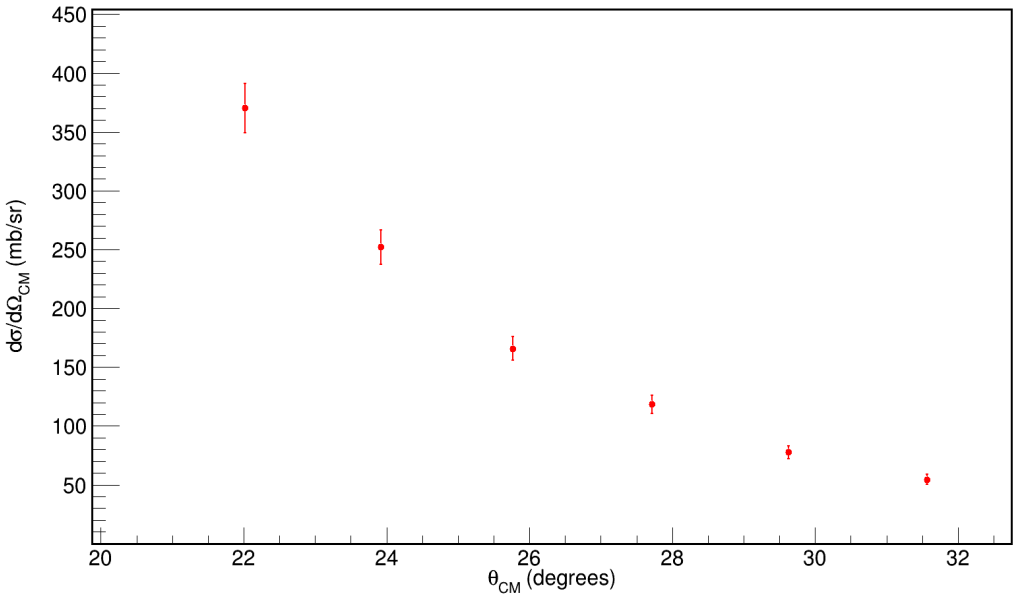

Figure 3.36: Differential cross section for ^{8}He$(d,d)^{8}$He(g.s.) in CM(center of mass) frame using S3 detector.

3.5.4 Differential cross section for the observed resonance state of the ^{8}He

In order to determine the peak position and width of the observed resonance, fitting of the overall spectrum is done using a total fit function that considers both the resonance width and the experimental resolution, while also accounting for background from non-resonant reaction channels. This total fit function which includes contributions from non-resonant reaction channels and an energy-dependent Voigt function can be seen Figure 3.38 with black line. The resonance state can be described using the Breit-Wigner distribution. Hence, in the excitation spectrum, the resonance state was fitted by combining a Gaussian function that takes into account the experimental resolution and Breit-Wigner distribution. The convolution of a Breit-Wigner distribution and a Gaussian function is a Voigt function. The Voigt function is a three-parameter distribution that includes the excitation energy of resonance peak (E_0), natural width (Γ) (FWHM), and resolution (σ).

$$P_{\text{Voigt}}(E;E_0,\Gamma,\sigma) = \int_{-\infty}^{\infty} \frac{e^{-(E_0)^2/(2\sigma^2)}}{\sigma\sqrt{2\pi}} \cdot \frac{\Gamma(E_r)/2}{\pi((E-E_0)^2+\Gamma(E_r)^2)/4}\, dE \tag{3.28}$$

where, first term under the integration is Gaussian function and second term is energy dependent Breit-Wigner distribution. The E is sum of the relative energy values of decay particles along x-axis of excitation spectrum and two-neutron separation energy. The width of Breit-Wigner distribution, which is dependent on energy ($\Gamma(E_r) = \Gamma_0\sqrt{(E/E_0)}$), was convoluted with the experimental resolution using a Voigt function. E_0 is the excitation energy of resonance peak.

The extracted peak position from the fitting of the newly observed state is 3.57 $\pm$ 0.02 MeV. The chi-square (χ^2) value of the fitting was found to be 1.03. The natural width (Γ) (FWHM) of Breit-Wigner distribution of the newly observed state is found to be 0.64 $\pm$ 0.06 MeV, where experimental resolution (σ= 0.210 MeV) was fixed while fitting. The experimental resolution was determined through simulations using the same parameters as those employed in the original experiment. The weighted average peak position is at 3.59 MeV and weighted average width (Γ) (FWHM) is 0.66 MeV of observed resonance state. The weighted average peak position and weighted average width values are consistent with the values obtained from full fit.

To determine the number of scattered deuterons, the excitation spectrum is generated for a set of four rings together for better statistics. Figure 3.39 shows the excitation spectrum (in blue) for one of the angular bins (rings 1-4) and scaled background from non-resonant reaction channels with uncertainty band (in green).

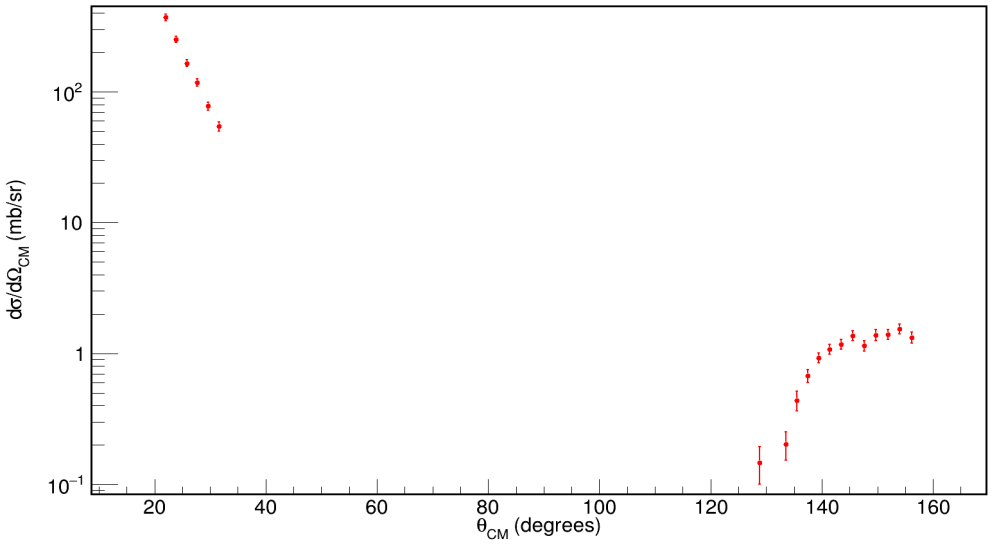

Figure 3.37: The differential cross section for ^{8}He(d,d)^{8}He(g.s) from the S3 and YY1 detectors in the CM frame.

The x-axis values, encompassing the range for which the integrated Voigt distribution achieves a 95% fill, are determined. The rest of the events in 5% area are also accounted. The green band, marked with vertical bars, represents uncertainty arising from non-resonant background channels and can be seen in Figure 3.39. The uncertainty band in a measurement is determined by Poisson statistics. The square root of the background counts provides an estimate of the statistical uncertainty. The integral over the upper portion of the band gives one set of background counts ($N_{upper}^{background}$), and the integral over the lower side gives another set ($N_{lower}^{background}$). Both sets are utilized in Equation 3.25 to calculate the uncertainty in the differential cross section. The maximum uncertainty, derived from $N_{upper}^{background}$, is employed to determine the uncertainty in the differential cross section. The deuteron counts were obtained for other bins too through a similar process. The relationship between θ_{cm} and θ_{lab} is shown in Figure 3.40.

The extracted differential cross section for the observed resonance state in the laboratory frame

and center-of-mass frame is shown in Figure 3.41 and 3.42 respectively.

Table 3.1 and table 3.3 summarizes the mean peak values, resolution and differential cross section values for the ^{8}He(d,d)^{8}He in the laboratory and center of mass (CM) frame for different angles of YY1 and S3 detector respectively. Table 3.2 and table 3.4 provides the total uncertainty, and statistical and systematical uncertainty values in the laboratory and center of mass (CM) frame for the ^{8}He(d,d)^{8}He in the laboratory and center of mass (CM) frame for different angles of YY1 and S3 detector respectively. Table 3.5 summarizes the mean peak values, natural width (Γ) (FWHM) and differential cross section for the ^{8}He(d,d') in the laboratory and center of mass (CM) frame for different angles of YY1. Table 3.6 provides the total uncertainty, and statistical and systematical uncertainty values in the laboratory and center of mass (CM) frame for the ^{8}He(d,d') in the laboratory and center of mass (CM) frame for different angles of YY1.

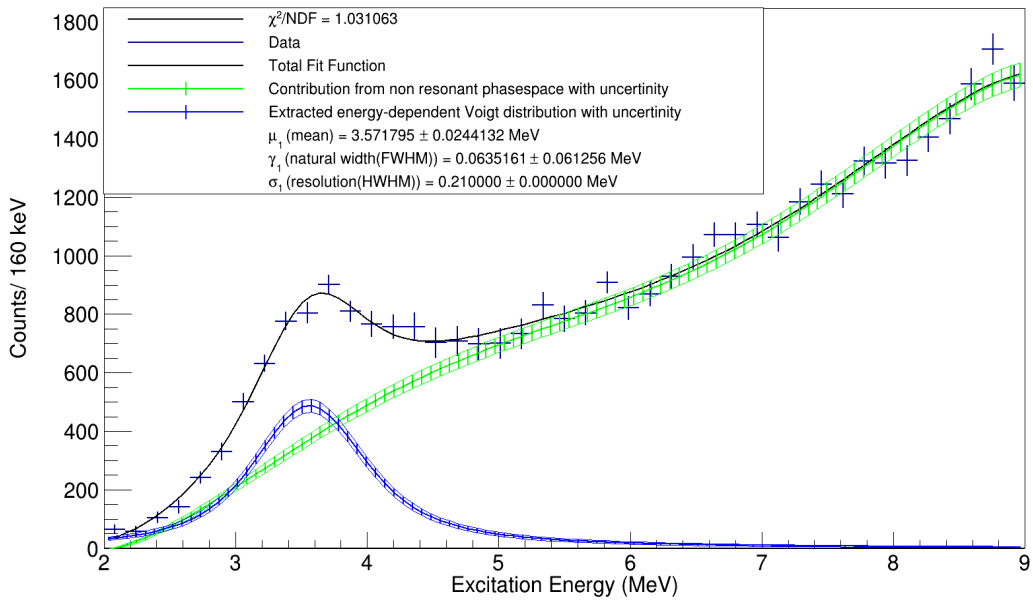

Figure 3.38: Excitation spectrum for non-elastic scattering with the background from Ag foil fitted with a function described in section 3.5 for all the rings of the YY1 detector.

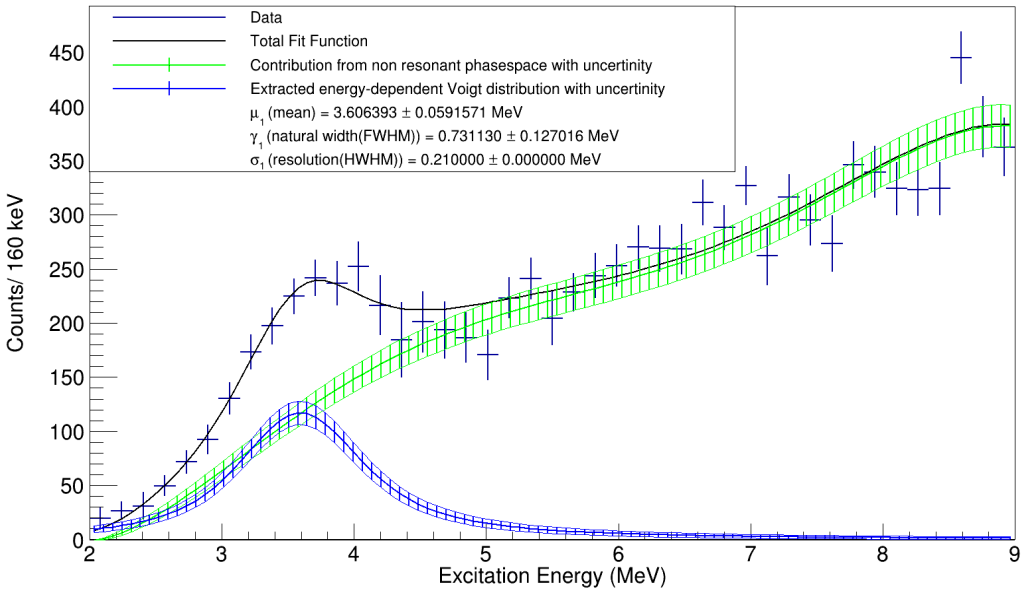

Figure 3.39: Excitation spectrum for non-elastic scattering for one of the angular bin (ring 1-4)

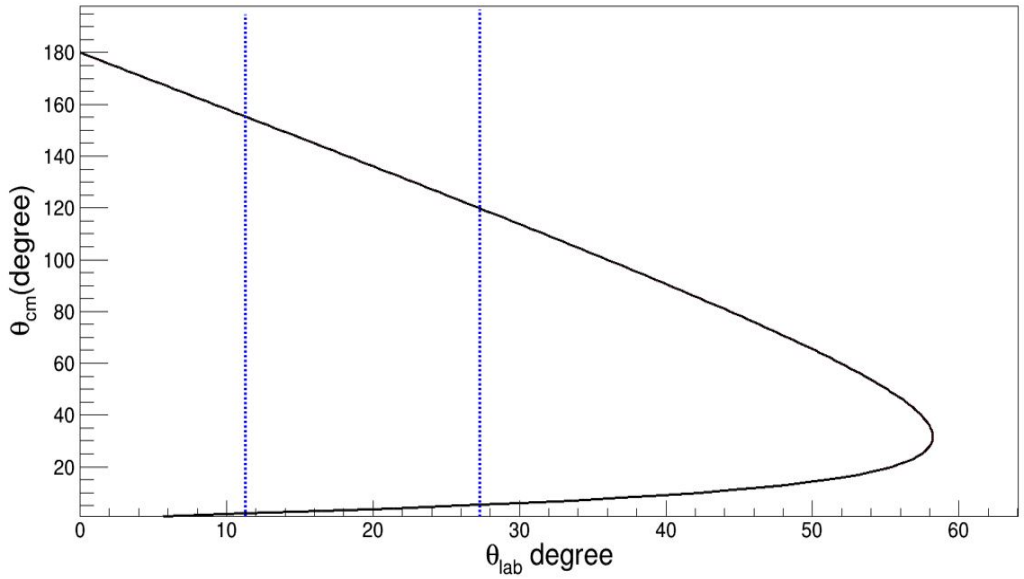

Figure 3.40: Relation between CM angle and laboratory angle for the observed resonance state. Detector coverage is shown by two vertical dashed lines.

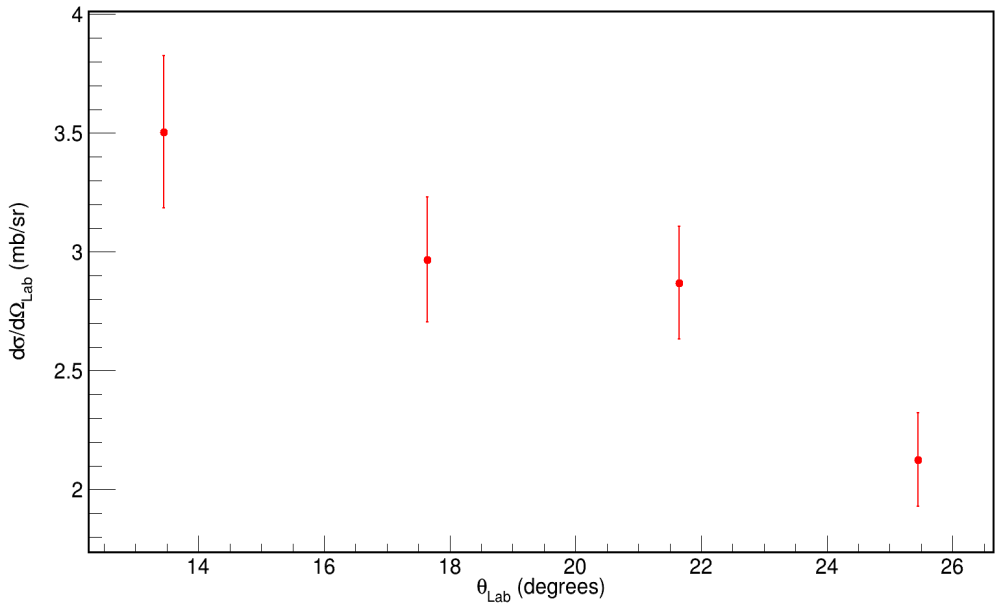

Figure 3.41: Differential cross section for the ^{8}He(d,d') in the laboratory frame.

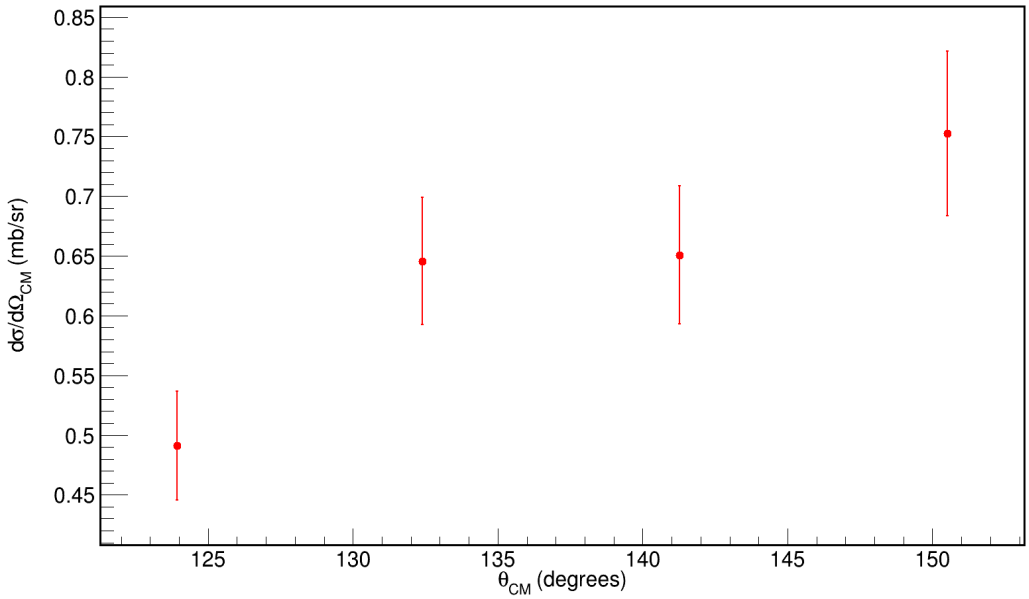

Figure 3.42: Differential cross section for the ^{8}He(d,d') in the CM frame.

θ_{Lab} (degrees)	θ_{CM} (degrees)	Ground State Peak (MeV)	Resolution ($\sigma\times$ 2.355) (FWHM) (MeV)	$\frac{d\sigma}{d\Omega_{\text{Lab}}}$ ($\frac{mb}{sr}$)	$\frac{d\sigma}{d\Omega_{\text{CM}}}$ ($\frac{mb}{sr}$)
11.85	156.17	0.014 ± 0.014	0.625 ± 0.030	5.2437	1.3257
12.93	154.00	0.020 ± 0.012	0.618 ± 0.025	6.0695	1.5417
14.00	151.85	0.026 ± 0.013	0.619 ± 0.028	5.4729	1.3957
15.06	149.72	0.044 ± 0.012	0.594 ± 0.025	5.4022	1.3854
16.11	147.61	0.034 ± 0.012	0.564 ± 0.028	4.4412	1.1447
17.15	145.52	0.056 ± 0.013	0.622 ± 0.023	5.2898	1.3712
18.18	143.45	0.042 ± 0.013	0.598 ± 0.030	4.5156	1.1775
19.19	141.41	0.025 ± 0.013	0.601 ± 0.028	4.1025	1.0768
20.20	139.40	-0.011 ± 0.012	0.601 ± 0.025	3.5051	0.9257
21.19	137.41	-0.051 ± 0.015	0.610 ± 0.026	2.5395	0.6751
22.16	135.45	-0.071 ± 0.024	0.733 ± 0.061	1.6373	0.4385
23.13	133.51	-0.065 ± 0.029	0.653 ± 0.062	0.7506	0.2025
25.45	128.81	-0.073 ± 0.031	0.601 ± 0.073	0.2661	0.1468

Table 3.1: Peak mean, resolution and differential cross section values for the ^{8}He(d,d)^{8}He elastic scattering in the laboratory and center of mass (CM) frame for different angles of YY1 detector.

θ_{Lab} (degrees)	θ_{CM} (degrees)	Statistical Uncertainty (CM) $(\frac{mb}{sr})$	Systematical Uncertainty (CM) $(\frac{mb}{sr})$	Total Uncertainty (Lab) $\Delta\frac{d\sigma}{d\Omega}$ $(\frac{mb}{sr})$	Total Uncertainty (CM) $\Delta\frac{d\sigma}{d\Omega}$ $(\frac{mb}{sr})$
11.85	156.17	0.1058	0.0665	0.4945	0.1250
12.93	154.00	0.1151	0.0774	0.5462	0.1387
14.00	151.85	0.0942	0.0700	0.4606	0.1174
15.06	149.72	0.1125	0.0695	0.5158	0.1322
16.11	147.61	0.0830	0.0574	0.3917	0.1009
17.15	145.52	0.0923	0.0688	0.4443	0.1151
18.18	143.45	0.0826	0.0591	0.3898	0.1016
19.19	141.41	0.0772	0.0540	0.3591	0.0942
20.20	139.40	0.0681	0.0464	0.3122	0.0824
21.19	137.41	0.0671	0.0339	0.2830	0.0752
22.16	135.45	0.0699	0.0220	0.2738	0.0733
23.13	133.51	0.0489	0.0101	0.1851	0.0499
25.45	128.81	0.0465	0.0073	0.0854	0.0471

Table 3.2: Total uncertainty, statistical and systematical uncertainty values for the ^{8}He(d,d)^{8}He elastic scattering in the laboratory and center of mass (CM) frame for different angles of YY1 detector.

θ_{Lab} (degrees)	θ_{CM} (degrees)	Ground State Peak (MeV)	Resolution ($\sigma\times$ 2.355) (FWHM) (MeV)	$\frac{d\sigma}{d\Omega_{\text{Lab}}}$ ($\frac{mb}{sr}$)	$\frac{d\sigma}{d\Omega_{\text{CM}}}$ ($\frac{mb}{sr}$)
4.36	22.02	0.024 ± 0.007	0.734 ± 0.010	9472.6568	370.2646
4.72	23.92	0.039 ± 0.009	0.732 ± 0.009	6477.4468	252.0467
5.08	25.82	0.021 ± 0.008	0.739 ± 0.011	4246.9743	164.4175
5.44	27.72	0.028 ± 0.011	0.736 ± 0.013	3074.0643	118.6546
5.80	29.63	0.035 ± 0.014	0.741 ± 0.020	2030.9755	77.7117
6.16	31.57	0.029 ± 0.017	0.745 ± 0.019	1431.9206	54.4250

Table 3.3: Peak mean, resolution and differential cross section values for the ^{8}He(d,d)^{8}He elastic scattering in the laboratory and center of mass (CM) frame for different angles of S3 detector.

θ_{Lab} (degrees)	θ_{CM} (degrees)	Statistical Uncertainty (CM) ($\frac{mb}{sr}$)	Systematical Uncertainty (CM) ($\frac{mb}{sr}$)	Total Uncertainty $\Delta\frac{d\sigma}{d\Omega_{\text{Lab}}}$ ($\frac{mb}{sr}$)	Total Uncertainty $\Delta\frac{d\sigma}{d\Omega_{\text{CM}}}$ ($\frac{mb}{sr}$)
4.36	22.02	10.1291	18.5930	541.6815	21.1731
4.72	23.92	7.1508	12.6566	373.5932	14.5370
5.08	25.82	5.6906	8.2563	259.0141	10.0274
5.44	27.72	4.7348	5.9432	197.3642	7.5987
5.80	29.63	3.7226	3.9023	140.9500	5.3932
6.16	31.57	3.1978	2.7329	110.6745	4.2065

Table 3.4: Total uncertainty, statistical and systematical uncertainty values for the ^{8}He(d,d)^{8}He elastic scattering in the laboratory and center of mass (CM) frame for different angles of S3 detector.

θ_{Lab} (degrees)	θ_{CM} (degrees)	Resonance Peak (MeV)	Natural Width (Γ) (FWHM) (MeV)	$\frac{d\sigma}{d\Omega_{\text{Lab}}}$ ($\frac{mb}{sr}$)	$\frac{d\sigma}{d\Omega_{\text{CM}}}$ ($\frac{mb}{sr}$)
13.45	150.52	3.60 ± 0.06	0.73 ± 0.12	3.5026	0.7526
17.64	141.27	3.55 ± 0.04	0.56 ± 0.09	2.9662	0.6508
21.65	132.4	3.67 ± 0.05	0.74 ± 0.09	2.8698	0.6455
25.45	123.93	3.62 ± 0.05	0.64 ± 0.12	2.1246	0.4914

Table 3.5: Natural width (Γ) (FWHM), resonance peak mean, and differential cross section values for the ^{8}He(d,d') inelastic scattering in the laboratory and center of mass (CM) frame for different angles.

θ_{Lab} (degrees)	θ_{CM} (degrees)	Statistical Uncertainty (CM) ($\frac{mb}{sr}$)	Systematical Uncertainty (CM) ($\frac{mb}{sr}$)	Total Uncertainty $\Delta\frac{d\sigma}{d\Omega_{\text{Lab}}}$ ($\frac{mb}{sr}$)	Total Uncertainty $\Delta\frac{d\sigma}{d\Omega_{\text{CM}}}$ ($\frac{mb}{sr}$)
13.45	150.52	0.0578	0.0377	0.3215	0.0690
17.64	141.27	0.0474	0.0326	0.2626	0.0576
21.65	132.4	0.0425	0.0324	0.2379	0.0535
25.45	123.93	0.0382	0.0246	0.1966	0.0454

Table 3.6: Total uncertainty, statistical and systematical uncertainty values for the ^{8}He(d,d') inelastic scattering in the laboratory and center of mass (CM) frame for different angles.

Chapter 4

Results and Discussion

This chapter describes the results obtained from the previous chapter. In the previous chapter, the excitation spectrum of ^{8}He was presented. One resonance state was observed along with the ground state. The first excited state was observed at excitation energy 3.57 $\pm$ 0.02 MeV with a natural width (Γ) (FWHM) of 0.64$\pm$ 0.06 MeV. This resonance state is consistent with the resonance at excitation energy 3.54 $\pm$ 0.06 MeV observed via ^{8}He(p,p') by M.Holl et al. [42] and that observed by Golovkov et al. [35] at excitation energy around 3.6 MeV via t(^{6}He,p)^{8}He. Apart from the ground state and the first excited state, no other excited state was observed in the excitation spectrum. A summary of findings of the excitation energy of the first exited state (2^{+}) from different studies can be seen in Figure 4.1.

The possible existence of a soft dipole mode in ^{8}He has been a controversial issue. A soft dipole resonance was observed at an excitation energy of around 4 MeV in an early experiment using the Coulomb excitation of ^{8}He [38, 39]. Later on, the low-lying spectrum of ^{8}He via a t(^{6}He,p)^{8}He transfer reaction was populated by Golovkov, Grigorenko, and collaborators and postulated that the near threshold spectrum to be explained by a low energy dipole strength function, which is

not necessarily a resonance state [35, 36]. From the theoretical perspective, a very recent *ab initio* work by Bonaiti, Bacca, and Hagan [40], addressed the possible existence of soft dipole mode in ^{8}He around 5 MeV, in agreement with refs [35, 36, 38, 39]. The reconstruction of excitation energy distribution of ^{8}He and momentum distributions of ^{6}He and neutrons from the dissociation experiment on ^{8}He performed at the National Superconducting Cyclotron Laboratory (NSCL) [51] and measurement of angular distribution in recent inelastic proton-scattering experiment concluded that the observed state was not consistent with dipole excitation [42]. The analysis of the ^{8}He(p,p') excitation spectrum was not in agreement with the dipole strength interpretation of Golovkov et al [35, 36]. Recently, the theoretical covariant density-functional theory (DFT) framework was used to compute ground-state properties and the dipole response of ^{8}He and concluded that the emergence of a soft dipole mode in ^{8}He is disfavored [41].

The comparison of findings of resonance width (FWHM) of first exited state (2^{+}) from different studies can be seen in Figure 4.2. The width of the observed resonance state is consistent with the other studies. It may be possible that absence of soft dipole resonance in the extracted excitation spectrum is due to the stronger binding of ^{8}He. There is also no intruder s-orbital known in ^{8}He which can allow L=1 particle-hole excitation.

The final goal of this study is to determine the spin of the observed resonance peak, based on the multipolarity of excitation. The extracted angular distribution for the ground state and first excited state was shown in the previous chapter. In order to determine the spin of the state, we will interpret angular distributions within the context of a one-step Distorted Wave Born Approximation (DWBA) calculation using the code FRESCO (Thompson,1988) [52]. The calculated elastic scattering cross section will be compared with our measured angular distribution for the ground state, allowing us to derive the optical potential parameters. By using these potential parameters,

the inelastic scattering angular distribution will be calculated for different multipolarities of excitation. The calculations that best fit with the data is determined as the multipolarity of excitation.

4.1 Summary

In this work, the deuteron inelastic scattering off a neutron halo nucleus, ^{8}He has been studied for the first time in inverse kinematics at IRIS facility at TRIUMF with beam energy 8.35A MeV. The excitation spectrum shows one resonance peak alongside with ground state. The resonance peak is observed at 3.57 $\pm$ 0.02 MeV with resonance width (Γ) of 0.64 $\pm$ 0.06 MeV (FWHM), which is consistent with the previous reported resonances. The differential cross sections for both the ground state and the observed resonance state were determined. The extracted differential cross section of observed resonance state will be compared with theoretical models to determine its spin, based on the multipolarity of the excitation.

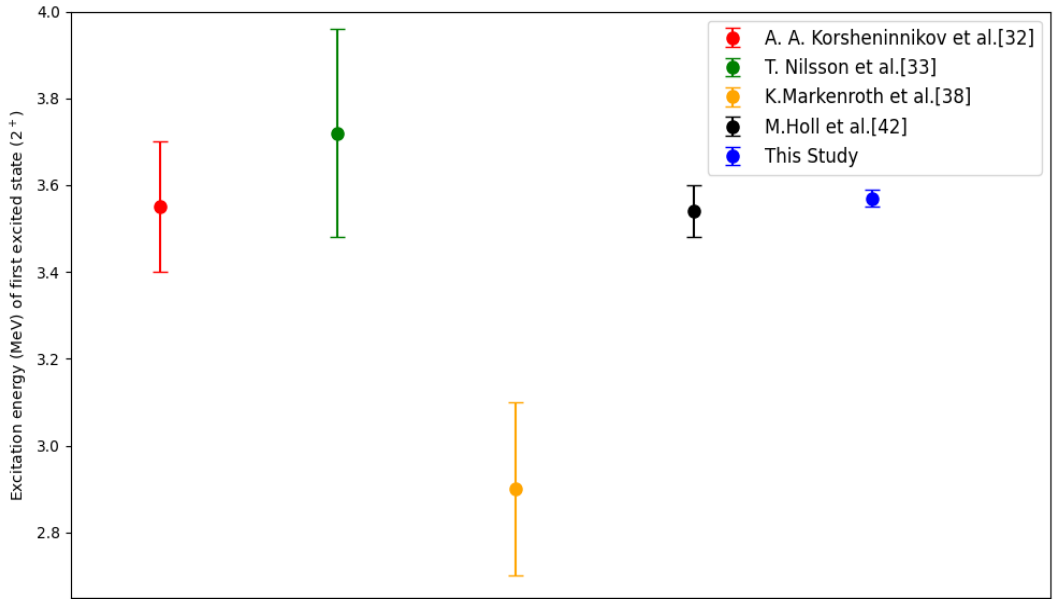

Figure 4.1: Summary of findings of first exited state (2^+) from different studies.

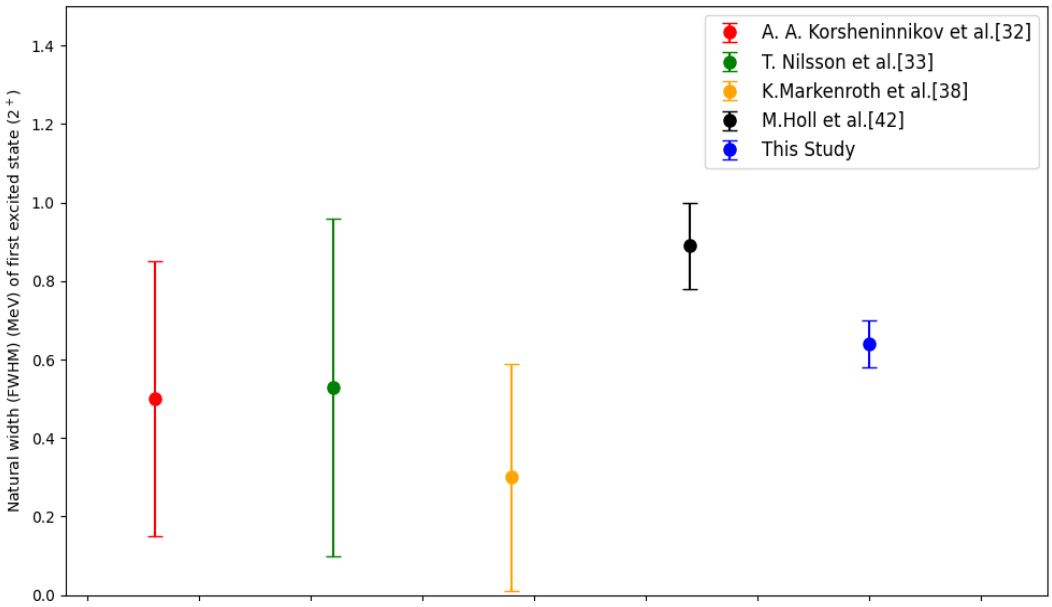

Figure 4.2: Comparison of findings of natural width (Γ) (FWHM) of first exited state (2^+) from different studies.

Bibliography

[1] I. Tanihata. Nuclear physics using unstable nuclear beams. *Hyperfine Interactions*, 21(1-4):251–264, 1985.

[2] I. Tanihata, H. Hamagaki, O. Hashimoto, et al. Measurements of interaction cross sections and radii of He isotopes. *Physics Letters B*, 160(6):380–384, 1985.

[3] M. G. Mayer. On closed shells in nuclei. II. *Physical Review*, 75(12):1969, 1949.

[4] H. Yukawa. On the interaction of elementary particles. *Proceedings of the Physico-Mathematical Society of Japan. 3rd Series*, 17:48–57, 1935.

[5] C. Lattes, H. Muirhead, G. Occhialini, et al. Processes involving charged mesons. *Nature*, 159(4047):694–697, 1947.

[6] https://www.nndc.bnl.gov/nudat3/.

[7] T. Yamaguchi, H. Koura, A. Litvinov, et al. Masses of exotic nuclei. *Progress in Particle and Nuclear Physics*, 120:103882, 2021.

[8] V. Weizsäcker. Zur theorie der kernmassen. *Zeitschrift für Physik*, 96(7-8):431–458, 1935.

[9] K. Krane. *Introductory nuclear physics*. John Wiley & Sons, 1991.

[10] P. Divyang. Literature Review (^{19}B).

[11] E. Shera, E. Ritter, R. Perkins, et al. Systematics of nuclear charge distributions in Fe, Co, Ni, Cu, and Zn deduced from muonic x-ray measurements. *Physical Review C*, 14(2):731, 1976.

[12] N. Bohr, H. Kramers, and J. Slater. London edinburgh dublin philosophical magazine. *J. Sci*, 47:785, 1924.

[13] A. Lakhtakia and E. Salpeter. Models and modelers of hydrogen. *American Journal of Physics*, 65(9):933–934, 1997.

[14] E. Caurier, G. Martínez-Pinedo, F. Nowacki, et al. The shell model as a unified view of nuclear structure. *Reviews of Modern Physics*, 77(2):427, 2005.

[15] M. G. Mayer. Nuclear configurations in the spin-orbit coupling model. ii. theoretical considerations. *Physical Review*, 78(1):22, 1950.

[16] O. Haxel, J. H. D. Jensen, and H. E. Suess. On the "magic numbers" in nuclear structure. *Physical Revview*, 75:1766–1766, 1949.

[17] R. Kanungo. A new view of nuclear shells. *Physica Scripta*, 2013(T152):014002, 2013.

[18] T. Otsuka. Exotic nuclei and nuclear forces. *Physica Scripta*, 2013(T152):014007, 2013.

[19] S. G. Zhou. Structure of exotic nuclei: a theoretical review. *arXiv preprint arXiv:1703.09045*, 2017.

[20] I. Tanihata, H. Hamagaki, A. Yamauchi, et al. Measurement of interaction cross sections for intermediate-energy He beams. *Physical Review Letters*, 60(9):692, 1988.

[21] P.G. Hansen and B. Jonson. The neutron halo of extremely neutron-rich nuclei. *Europhysics Letters*, 4(4):409, 1987.

[22] T. Kobayashi, S. Shimoura, T. Tanihata, et al. Electromagnetic dissociation and soft giant dipole resonance of the neutron-dripline nucleus ^{11}Li. *Physics Letters B*, 232(1):51–55, 1989.

[23] P.G. Hansen, A.S. Jensen, and B. Jonson. Nuclear halos annual review. *Rev. Nucl. Part. Sci*, 45:591, 1995.

[24] A.S. Jensen and K. Riisager. Towards necessary and sufficient conditions for halo occurrence. *Physics Letters B*, 480(1-2):39–44, 2000.

[25] M. Zhukov, B. Danilin, D. Fedorov, et al. Bound state properties of Borromean halo nuclei: ^{6}He and ^{11}Li. *Physics Reports*, 231(4):151–199, 1993.

[26] I. Tanihata, D. Hirata, T. Kobayashi, et al. Revelation of thick neutron skins in nuclei. *Physics Letters B*, 289(3-4):261–266, 1992.

[27] O. Bochkarev, L. Chulkov, P. Egelhof, et al. Evidence for a neutron skin in ^{20}N. *The European Physical Journal A-Hadrons and Nuclei*, 1:15–17, 1998.

[28] J. Al-Khalili. An introduction to halo nuclei. In *The Euroschool Lectures on Physics with Exotic Beams, Vol. I*, pages 77–112. Springer Berlin Heidelberg Berlin, Heidelberg, 2004.

[29] T. Aumann, W. Bartmann, O. Boine-Frankenheim, et al. Puma, antiproton unstable matter annihilation. *Eur. Phys. J.*, 58:88, 2022.

[30] S. Pieper, R. Wiringa, and J. Carlson. Quantum monte carlo calculations of excited states in A = 6–8 nuclei. *Physical Review C*, 70(5):054325, 2004.

[31] W. Oertzen, H. Bohlen, B. Gebauer, et al. Nuclear structure studies of very neutron-rich isotopes of $^{7-10}$He, $^{9-11}$ Li and $^{12-14}$Be via two-body reactions. *Nuclear Physics. A*, 588(1):129–134, 1995.

[32] A. Korsheninnikov, D. Aleksandrov, N. Aoi, et al. Experimental studies of light neutron-rich nuclei. *Nuclear Physics A*, 588(1):23–28, 1995.

[33] T. Nilsson, F. Humbert, W. Schwab, et al. ^{6}He and neutron momentum distributions from ^{8}He in nuclear break-up reactions at 240 MeV/u. *Nuclear Physics A*, 598(3):418–434, 1996.

[34] X. Jun, Y. Yan-Lin, C. Zhong-Xin, et al. New Measurements for ^{8}He Excited States. *Chinese Physics Letters*, 29, 2012.

[35] M. Golovkov, L. Grigorenko, G. Ter-Akopian, et al. The ^{8}He and ^{10}He spectra studied in the (t, p) reaction. *Physics Letters B*, 672(1):22–29, 2009.

[36] L. Grigorenko, M. Golovkov, G. Ter-Akopian, et al. Soft dipole mode in ^{8}He. *Physics of Particles and Nuclei Letters*, 6:118–125, 2009.

[37] M. V. Zhukov, A. A. Korsheninnikov, and M. H. Smedberg. Simplified α+4n model for the ^{8}He nucleus. *Phys. Rev. C*, 50:R1–R4, Jul 1994.

[38] K. Markenroth, M. Meister, B. Eberlein, et al. ^{8}He–^{6}He: a comparative study of nuclear fragmentation reactions. *Nuclear Physics A*, 679(3-4):462–480, 2001.

[39] M. Meister, K. Markenroth, D. Aleksandrov, et al. ^{8}He–^{6}He: a comparative study of electromagnetic fragmentation reactions. *Nuclear Physics A*, 700(1-2):3–16, 2002.

[40] F. Bonaiti, S. Bacca, and G. Hagen. Ab initio coupled-cluster calculations of ground and dipole excited states in ^{8}He. *Phys. Rev. C*, 105:034313, 2022.

[41] J. Piekarewicz. Insights into the possible existence of a soft dipole mode in ^{8}He. *Phys. Rev. C*, 105:044310, Apr 2022.

[42] M. Holl, R. Kanungo, Z. Sun, et al. Proton inelastic scattering reveals deformation in ^{8}He. *Physics Letters B*, 822:136710, 2021.

[43] R. Kanungo, H. Savajols, T. Roger, et al. New evidence of soft dipole resonance in ^{11}Li. In *12th International Conference on Nucleus-Nucleus Collisions*, 2015.

[44] Maria Jose Garcia Borge. ISOL-based and Fragmentation-based Production of Rare Isotope Beams. https://epistemia.nucleares.unam.mx/uploads/ckeditor/attachments/474/summary-production_Nuclei-v1.pdf. CERN.

[45] R. Kanungo. IRIS: The ISAC charged particle reaction spectroscopy facility for reaccelerated high-energy ISOL beams. *Hyperfine Interactions*, pages 235–240, 2014.

[46] M. Singh. Investigation of resonance states in ^{11}Li.

[47] https://www.mesytec.com/products/nuclear-physics/MSCF-16_F_V.html.

[48] A. Kumar. Investigating the three-nucleon force through ^{10}C(p,p)^{10}.

[49] R. Brun and F. Rademakers. ROOT - An Object Oriented Data Analysis Framework. *Nucl. Inst. & Meth. in Phys. Res. A*, 389:81–86, 1997.

[50] ROOT [software], release v6.26/10, 16/11/2022.

[51] Y. Iwata, K. Ieki, A. Galonsky, J. J. Kruse, et al. Dissociation of ^{8}He. *Phys. Rev. C*, 62:064311, 2000.

[52] I. Thompson. Coupled reaction channels calculations in nuclear physics. *Computer Physics Reports*, 7(4):167–212, 1988.